



# A T cell resilience model associated with response to immunotherapy in multiple tumor types

Yu Zhang<sup>1,2,3,14</sup>, Trang Vu<sup>1,14</sup>, Douglas C. Palmer<sup>4,11</sup>, Rigel J. Kishton<sup>4,12</sup>, Lanqi Gong<sup>2</sup>, Jiao Huang<sup>ID 2</sup>, Thanh Nguyen<sup>5,13</sup>, Zuojia Chen<sup>6</sup>, Cari Smith<sup>7</sup>, Ferenc Livák<sup>8</sup>, Rohit Paul<sup>9</sup>, Chi-Ping Day<sup>ID 10</sup>, Chuan Wu<sup>6</sup>, Glenn Merlino<sup>ID 10</sup>, Kenneth Aldape<sup>ID 5</sup>, Xin-yuan Guan<sup>ID 2</sup> and Peng Jiang<sup>ID 1✉</sup>

**Despite breakthroughs in cancer immunotherapy, most tumor-reactive T cells cannot persist in solid tumors due to an immunosuppressive environment. We developed Tres (tumor-resilient T cell, <https://resilience.ccr.cancer.gov/>), a computational model utilizing single-cell transcriptomic data to identify signatures of T cells that are resilient to immunosuppressive signals, such as transforming growth factor-β1, tumor necrosis factor-related apoptosis-inducing ligand and prostaglandin E2. Tres reliably predicts clinical responses to immunotherapy in melanoma, lung cancer, triple-negative breast cancer and B cell malignancies using bulk T cell transcriptomic data from pre-treatment tumors from patients who received immune-checkpoint inhibitors ( $n = 38$ ), infusion products for chimeric antigen receptor T cell therapies ( $n = 34$ ) and pre-manufacture samples for chimeric antigen receptor T cell or tumor-infiltrating lymphocyte therapies ( $n = 84$ ). Further, Tres identified *FIBP*, whose functions are largely unknown, as the top negative marker of tumor-resilient T cells across many solid tumor types. *FIBP* knockouts in murine and human donor CD8<sup>+</sup> T cells significantly enhanced T cell-mediated cancer killing in *in vitro* co-cultures. Further, *Fibp* knockout in murine T cells potentiated the *in vivo* efficacy of adoptive cell transfer in the B16 tumor model. *Fibp* knockout T cells exhibit reduced cholesterol metabolism, which inhibits effector T cell function. These results demonstrate the utility of Tres in identifying biomarkers of T cell effectiveness and potential therapeutic targets for immunotherapies in solid tumors.**

Cancer immunotherapies that act through T cells have led to significant successes. Immune-checkpoint inhibitors (ICIs) that block CTLA4 and PD-1/PD-L1 signaling can induce responses in 10–35% of patients with diverse tumor types, such as melanoma, non-small cell lung, head neck, gastric, bladder, urinary, kidney and liver cancer<sup>1</sup>. Similarly, the adoptive transfer of expanded tumor-infiltrating lymphocytes (TILs) has led to durable responses in 20–25% of patients with metastatic melanoma<sup>2</sup>. Cellular immunotherapies also include T cell receptor (TCR)<sup>3</sup> or chimeric antigen receptor (CAR) T cells<sup>4</sup> engineered to recognize cell-surface targets on malignant cells. However, most patients with solid tumors do not respond to ICI or TIL therapies<sup>1,2</sup> and CAR-T therapy is only effective in hematological cancers but not solid tumors<sup>5</sup>.

Even after therapeutic interventions, the tumor microenvironment may suppress antitumor T cells through mechanisms other than CTLA4 and PD-1–PD-L1 signaling, such as alternative checkpoints, immunosuppressive cells or cytokine and metabolite release<sup>6</sup>. T cells may also lose antitumor activities due to cell-intrinsic mechanisms that act independently of other immunosuppressive factors. For example, CAR-T cells may progressively upregulate Fas ligand, tumor necrosis factor (TNF)-related apoptosis-inducing ligand (TRAIL) and their cognate receptors, resulting in cell death<sup>7</sup>. Such

activation-induced T cell death is essential for maintaining immune tolerance and homeostasis<sup>8</sup> but may limit the long-lasting effect of cell therapy. Therefore, developing new cancer immunotherapies requires understanding molecular characteristics of T cells with high or low antitumor efficacies.

With this goal in mind, studies have collected single-cell T cell transcriptomes from ICI-treated melanoma or lung tumors to identify the molecular signatures of T cells associated with favorable or unfavorable clinical outcomes<sup>9,10</sup>. Additional studies have analyzed single T cell transcriptomes from tumors without associated therapy outcomes<sup>11</sup>, although methods for identifying signatures of effective antitumor T cells from studies without treatment information have yet to be developed.

Functional genomics screens have also contributed to understanding the molecular programs underlying T cell effectiveness. For example, genome-wide CRISPR screens in human donor T cells have identified many regulators of T cell proliferation upon TCR stimulation<sup>12</sup> and nuclear factor (NF)-κB pathways in promoting interferon (IFN)-γ cytokine production<sup>13</sup>. Open reading frame (ORF) screens can even explore the potential of overexpressing genes absent in lymphocytes on enhancing T cell effector functions<sup>14</sup>. However, *in vitro* T cell proliferation or cytokine levels in genome-wide CRISPR or ORF screens<sup>12,13</sup> are not directly

<sup>1</sup>Cancer Data Science Laboratory, Center for Cancer Research, National Cancer Institute, National Institutes of Health, Bethesda, MD, USA. <sup>2</sup>Department of Clinical Oncology, The University of Hong Kong, Hong Kong, China. <sup>3</sup>Sun Yat-sen University Cancer Center, State Key Laboratory of Oncology in South China, Collaborative Innovation Center for Cancer Medicine, Guangzhou, China. <sup>4</sup>Surgery Branch, National Cancer Institute, National Institutes of Health, Bethesda, MD, USA. <sup>5</sup>Laboratory of Pathology, Center for Cancer Research, National Cancer Institute, National Institutes of Health, Bethesda, MD, USA.

<sup>6</sup>Experimental Immunology Branch, Center for Cancer Research, National Cancer Institute, National Institutes of Health, Bethesda, MD, USA. <sup>7</sup>Laboratory Animal Science Program, Leidos Biomedical Research Inc, Frederick, MD, USA. <sup>8</sup>Flow Cytometry Core, Center for Cancer Research, National Cancer Institute, National Institutes of Health, Bethesda, MD, USA. <sup>9</sup>Office of the Director, Center for Cancer Research, National Cancer Institute, National Institutes of Health, Bethesda, MD, USA. <sup>10</sup>Laboratory of Cancer Biology and Genetics, Center for Cancer Research, National Cancer Institute, National Institutes of Health, Bethesda, MD, USA. <sup>11</sup>Present address: AstraZeneca, Gaithersburg, MD, USA. <sup>12</sup>Present address: Lyell Immunopharma, South San Francisco, CA, USA. <sup>13</sup>Present address: Gaia Foods, Singapore, Singapore. <sup>14</sup>These authors contributed equally: Yu Zhang, Trang Vu. ✉e-mail: peng.jiang@nih.gov

measuring the antitumor capability. In vivo genetic screens address these limitations by pooling genes to evaluate gene inhibition effects on the T cell accumulation in murine tumors<sup>15</sup>. However, murine tumors can host only a limited number of T cells tagged with guide RNAs (gRNAs). Therefore, most genes receive a ‘zero’ count in a genome-wide screen and are dropped from further evaluation;<sup>16</sup> thus, such a screen may miss many authentic regulators of T cell antitumor functions.

To overcome the limitations discussed above, we developed a computational framework named Tres to identify CD8<sup>+</sup> T cells that are resilient to immunosuppressive signals in solid tumors<sup>17</sup>. The Tres model, trained using single-cell data from tumors not subjected to any immunotherapy, can reliably predict the clinical efficacies of ICI or cellular therapies. Further, the Tres model revealed *FIBP* as a negative marker of T cell antitumor efficacy and a potential therapeutic target. Together, our study presents a data-driven framework to discover biomarkers and therapeutic targets for T cell immunotherapies in solid tumors.

## Results

**Quantification of immunosuppression on CD8<sup>+</sup> T cells.** Tres uses two stages to identify gene markers of CD8<sup>+</sup> T cells that are resilient to immunosuppressive signals in solid tumors (Fig. 1a). The Tres model first quantifies the level of immunosuppression imposed on the CD8<sup>+</sup> T cells in a single-cell transcriptomic dataset as the signaling activities of immunosuppressive cytokines (stage 1; Fig. 1a). The basis for this calculation can be illustrated by a melanoma tumor example<sup>18</sup>, where transforming growth factor (TGF)- $\beta$ 1 signaling activities in CD8<sup>+</sup> T cells, computed by CytoSig<sup>19</sup>, negatively correlate with T cell proliferation levels, inferred by the expression of cell cycle and DNA replication genes<sup>20</sup> (Fig. 1b). We identified a consistent anti-correlation between TGF- $\beta$ 1 signaling activity and T cell proliferation in 168 tumors from 36 single-cell RNA-sequencing (RNA-seq) datasets spanning 19 cancer types (Extended Data Fig. 1a, left and Supplementary Table 1).

Similarly, CytoSig-predicted TRAIL and prostaglandin E2 (PGE2) signaling activities correlate with low T cell proliferation across single-cell transcriptomic datasets (Extended Data Fig. 1a, left). This result is consistent with the function of TRAIL signaling in promoting activation-induced T cell death<sup>7</sup> and the function of PGE2-cAMP signaling in suppressing T effector cells<sup>21</sup>. The negative correlations between signaling activities and T cell proliferation for immunosuppressive cytokines are more significant than correlations for T cell effector cytokines IFN- $\gamma$  and TNF (Extended Data Fig. 1a, left).

In contrast to T cell proliferation, cytotoxicity scores (computed by granzyme and perforin expression) do not show significant negative correlations with CytoSig-predicted signaling activities (Extended Data Fig. 1a, middle). Also, unlike signaling activities, expression levels of TGF- $\beta$ 1, TRAIL and PGE2 receptors do not correlate with T cell proliferation (Extended Data Fig. 1a, right). These results suggested the necessity of CytoSig in quantifying immunosuppression on T cell proliferation. As a further quality control, we evaluated the consistency between TGF- $\beta$ 1, TRAIL and PGE2 signaling activities and each signal’s known downstream activities and found CytoSig predictions to be reliable (Extended Data Fig. 1b-f). Diverse cell populations in tumors, such as monocytes and cancer cells, are potential producers of these signals (Extended Data Fig. 1g).

CytoSig also predicts the activities of other potential immunosuppressive cytokines, such as interleukin (IL)-10, IL-4 and vascular endothelial growth factor A (VEGFA). However, IL-10 (ref. <sup>22</sup>) and IL-4 (ref. <sup>23</sup>) may potentiate T cell antitumor functions, and VEGFA activities predicted by CytoSig do not correlate with T cell proliferation (Methods and Extended Data Fig. 1a, left). These results deterred us from including additional cytokines in the

model. Thus, in later analyses, the Tres model focuses on three key immunosuppressive signals, TGF- $\beta$ 1, TRAIL and PGE2, which modulate T cell proliferation.

**Transcriptomic marker genes of tumor-resilient T cells.** After the immunosuppression quantification for each T cell, the second Tres stage utilizes a variable interaction test to identify gene expression markers of T cells that are resilient to the previously identified inhibitive signals (TGF- $\beta$ 1, TRAIL or PGE2) in solid tumors (Fig. 1a). The Tres model searches for genes whose expression status mitigates the negative correlation between immunosuppression and T cell proliferation across T cells. For instance, in our previous example from a melanoma tumor, we found that the negative correlation between immunosuppression and T cell proliferation is evident only for T cells with low *IL7R* or high *FIBP* expression levels (Fig. 1c and Extended Data Fig. 2a).

Relationships between immunosuppression, T cell proliferation and the expression status of a third gene can be evaluated through the interaction covariate in linear regression (Supplementary Table 2 and Methods). Therefore, we defined the interaction test *t* values (Coef/StdErr) as each gene’s Tres score. A positive Tres score for a gene indicates that T cells with positive expression for that gene maintain similar proliferative values even under suppression from TGF- $\beta$ 1, TRAIL or PGE2 signaling (*IL7R* example in Fig. 1c). A negative Tres score for a gene indicates that T cells with positive expression for that gene do not proliferate under suppressions from TGF- $\beta$ 1, TRAIL or PGE2 signaling (*FIBP* example in Fig. 1c). The interaction test *P* values indicate the statistical significance of Tres scores (Extended Data Fig. 2b).

To evaluate the Tres model, we assembled 36 single-cell RNA-seq datasets from 168 tumors spanning 19 cancer types, wherein each tumor consisted of at least 100 single T cell transcriptomes (Supplementary Table 1). Each tumor has a Tres signature, consisting of one Tres score for each gene. For example, the previously mentioned *IL7R* and *FIBP* genes have consistently positive and negative Tres scores across tumors, respectively (Fig. 1d). Further, Tres scores for immune-checkpoint genes are negative, whereas Tres scores for T cell persistence or activation markers are positive across tumors (Extended Data Fig. 2c). In contrast, Tres scores for immunosuppressive signal receptors are not significant (Extended Data Fig. 2d), suggesting that the single-cell expression of receptors may not be an indicator of cytokine activity. Generally, Tres scores from diverse cohorts are positively correlated with each other (Extended Data Fig. 2e).

Using any one of three immunosuppressive signals TGF- $\beta$ 1, TRAIL and PGE2, the model achieved statistical significance (>0.1% genes with Tres scores false discovery rate (FDR)<0.05; Methods) in at least 130 out of 168 tumors (Supplementary Table 1). We focused our analyses on these 130 tumors with significant Tres scores.

**Tres signatures identify marker genes of T cell persistence.** To validate the biological relevance of the Tres model, we evaluated whether Tres signatures can predict previously defined T cell persistence markers. A recent study of adoptive transfer of TILs identified a T cell-persistence gene signature based on the transcriptomic profiles of stem-like CD8<sup>+</sup> T cells associated with complete cancer regression and TIL persistence in tumors<sup>24</sup>. Our Tres gene scores reliably captured top markers in the T cell-persistence signature (Fig. 1e,f and Extended Data Fig. 2f,g). We found that median Tres signatures merged from all immunosuppressive signals achieved the highest performance (Extended Data Fig. 2g). As a control, we applied the Tres model on transcriptomic data generated from in vitro cultures of cancer cell lines and found that result performance is close to random, as expected (Extended Data Fig. 2h).

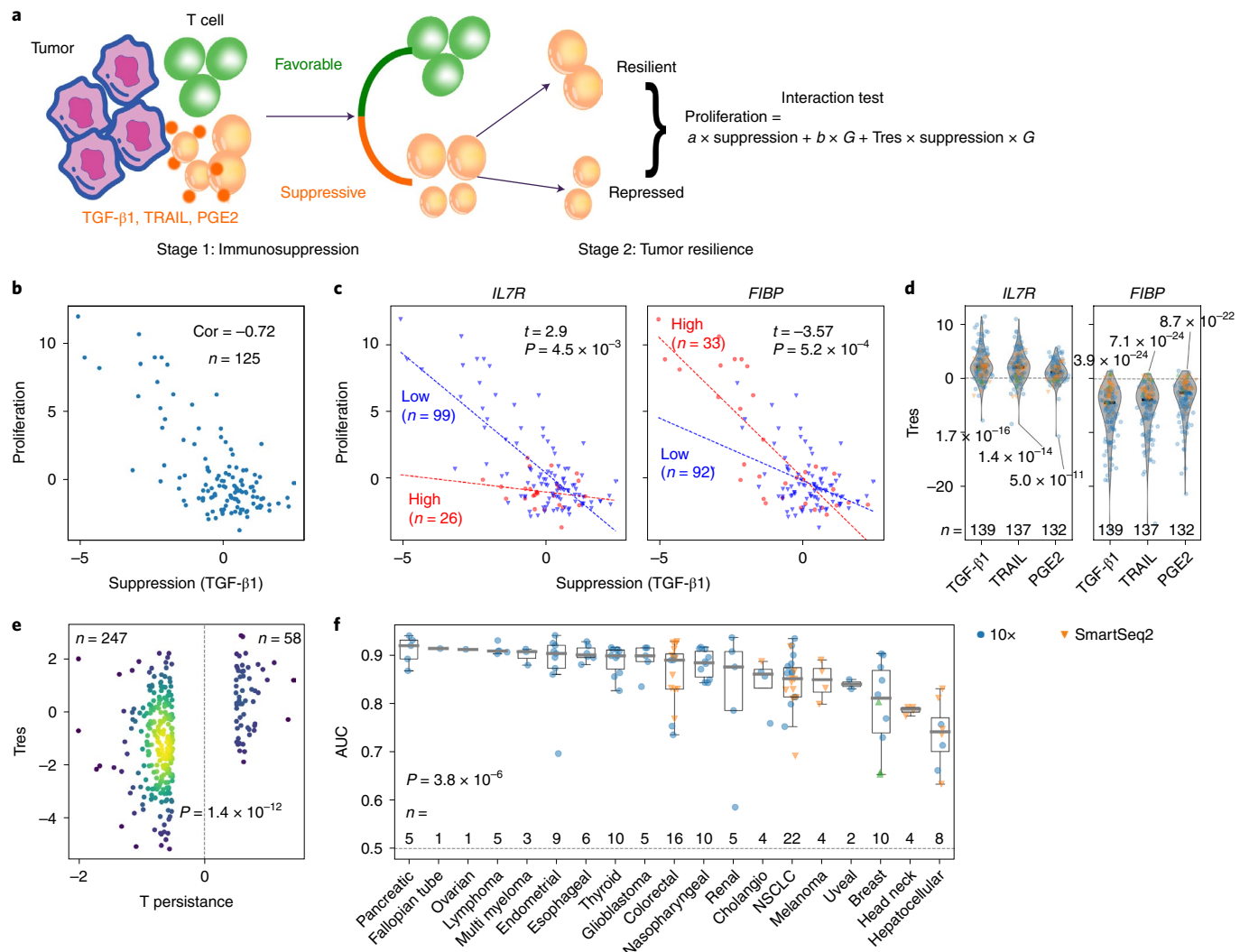


**Fig. 1 | Modeling transcriptomic signatures of tumor-resilient T cells.** **a**, Two stages of identifying tumor-resilient T cells. Using single-cell RNA-seq data as inputs, Tres first quantifies the immunosuppression level on each T cell based on signaling activities of TGF- $\beta$ 1, TRAIL and PGE2. Then, Tres identifies gene signatures associated with T cells that are still proliferative under immunosuppressive signals through an interaction test. **b**, Negative correlation between immune suppression and T cell proliferation, an example from a melanoma tumor<sup>18</sup>. Each dot represents a CD8<sup>+</sup> T cell. The x axis shows immunosuppression as TGF- $\beta$ 1-signaling activities. The y axis shows cell proliferation scores computed through cell cycle and DNA replication genes. **c**, Tres scores from the variable interaction test. The correlation between immune suppression and T cell proliferation is plotted the same as **b**, except that cells were split into high and low groups according to *IL7R* or *FIBP* expression (cutoff of 2). The t value (Tres score) and P value were computed through the two-sided interaction test using continuous values without any cutoffs. **d**, Tres score distributions across many cohorts. Each dot represents a tumor. Tres scores computed for each signal are shown through violin plots smoothed by a kernel density estimator. P values (with sample counts labeled on each group) were from the two-sided Wilcoxon signed-rank test comparing group values and zero. **e**, Association between Tres and T cell persistence scores, example from a melanoma tumor<sup>18</sup>. Each dot presents a gene with the median Tres score among TGF- $\beta$ 1, TRAIL and PGE2 signals on the y axis and the T cell persistence score<sup>24</sup> on the x axis. The P value was from the two-sided Wilcoxon rank-sum test, comparing the Tres scores between genes with positive and negative T cell persistence scores. **f**, Quality of Tres scores in different cancers. Each dot represents a tumor with the ROC AUC on the y axis, with 0.5 as the random expectation. The thick line represents the median value. The bottom and top of the boxes are the 25th and 75th percentiles, respectively (interquartile range). Whiskers encompass 1.5 times the interquartile range. The P value was from the two-sided Wilcoxon signed-rank test, comparing group medians and zero. NSCLC, non-small cell lung cancer.

Gene set enrichment analysis (GSEA) revealed the positive regulation of  $\alpha\beta$  T cell proliferation<sup>25</sup> as the most enriched pathway in Tres signatures (Extended Data Fig. 3a,b). The top gene supporting this enrichment is *HLA-E*, which represses natural killer (NK) cells through the NKG2A receptor<sup>26</sup>. Tres predicted the *HLA-E* as a positive marker of tumor-resilient T cells (Extended Data Fig. 3c), corroborating the protective role of *Qa1* (mouse ortholog of *HLA-E*) expressed by activated T cells against NK-cell mediated T cell lysis<sup>27,28</sup>.

**Tres signature correlations predict immunotherapy outcomes.** To validate the clinical relevance of the Tres model, we evaluated Tres signatures on predicting the effectiveness of T cells in cancer immunotherapies (procedure in Extended Data Fig. 4a). We trained a median Tres signature using immunotherapy-naïve single-cell RNA-seq datasets collected from public repositories<sup>18,29–39</sup> (Supplementary Table 1) and used this median Tres signature in all further analyses. As validation data, we used published single-cell transcriptomic profiles of T cells from responders and

non-responders to ICIs in melanoma<sup>9</sup>, triple-negative breast cancer (TNBC)<sup>40</sup>, basal cell carcinoma<sup>41</sup> and non-small cell lung cancer<sup>10</sup> and created a bulk T cell transcriptomics profile averaged across all single T cell data for each patient.

Although the Tres signature training does not involve any immunotherapy information, the median Tres signature correlates better with T cell transcriptomic profiles from pretreatment tumors<sup>9,40,41</sup> (Fig. 2a) and post-treatment tumors<sup>9,10</sup> (Extended Data Fig. 4b) in ICI responders than with profiles from non-responders. Compared to many published signatures of T cell antitumor efficacy<sup>12,15,24,42–45</sup> (Supplementary Table 3), the performance of the Tres signature is generally the best (Fig. 2b and Extended Data Fig. 4c), although a T memory stem cell (Tscm)<sup>42</sup> signature performs better in two out of six cases. On average, Tres is the most predictive signature (Fig. 2c and Extended Data Fig. 4d).

Single-cell profiling remains uncommon in clinical practice due to its high cost and requirement for high-quality samples. Therefore, we evaluated the median Tres signature using bulk-tumor profiles for T cell expansion before adoptive cell therapy in melanoma<sup>46</sup>. Among tumor profiles with high cytotoxic T cell infiltration, correlations between the Tres signature and bulk-tumor expression profiles can reliably predict survival outcomes (Fig. 2d). However, if the T cell infiltration level is low in bulk tumors, the Tres signature becomes non-predictive (Extended Data Fig. 4e). Similarly, using bulk-tumor transcriptomes, Tres predicted ICI outcome at the highest accuracy when the intratumoral T cell infiltration is high, although the accuracy may not be significant for specific cohorts (Extended Data Fig. 4f and Supplementary Table 4). These results are expected because the Tres signature training uses only T cell transcriptomes, which are not enriched in tumors with low T cell infiltration and can be interfered with by non-lymphocyte populations even in T cell inflamed tumors.

As further controls, the median Tres signature is not predictive of clinical outcome using T cell transcriptomic profiles from peripheral blood of ICI-treated patients or tumors treated with only chemotherapies (Extended Data Fig. 4g). Also, the Tres signature cannot predict ICI outcome using bulk expression data from tumors with low expression of immunosuppressive signals (Extended Data Fig. 4h). Together, these results indicate the specificity of Tres on modeling intratumoral T cell resilience to suppressive signals in cancer immunotherapies.

Although the Tres model was developed to analyze solid tumors, the median Tres signature is predictive of anti-CD19 CAR-T response in hematopoietic malignancies. We analyzed clinical studies of CD19 CAR-T efficacy, measured by the patient response in chronic lymphocytic leukemia<sup>47</sup> or the duration of B cell aplasia in acute lymphoblastic leukemia<sup>48</sup>. The correlation between Tres signature and bulk T cell transcriptomic profiles from infusion products (Fig. 2a,b bottom) or before CAR-T manufacture (Fig. 2e) is significantly predictive of therapy response.

In summary, compared to published signatures of T cell antitumor efficacy<sup>12,15,24,42–45</sup> (Supplementary Table 3), the performance of the median Tres signature is consistently the best at predicting binary response (Fig. 2c and Extended Data Fig. 4d) using ICI pre-treatment tumor samples ( $n=38$  patients) and CAR-T infusion products ( $n=34$  patients) or survival durations (Fig. 2f) using pre-manufacture samples for CAR-T or TIL therapies ( $n=84$  patients). These results suggest that Tres could be used to screen patients before the start of immunotherapy (Supplementary Table 5).

Currently, the most well-established biomarkers for ICIs are tumor mutation burden (TMB) and tumor PD-L1 levels assessed by immunohistochemistry (IHC). A systematic meta-analysis of anti-PD-1/PD-L1 biomarkers across ten solid tumor types in 8,135 patients reported the area under the receiver-operating characteristic (ROC) curve (AUC) of PD-L1 IHC and TMB as 0.65 and 0.69, respectively<sup>49</sup>. Another meta-analysis that reprocessed

whole-exome data over 1,000 ICI-treated patients across seven tumor types reported the AUC of TMB as  $0.63 \pm 0.05$  (ref. <sup>50</sup>). The mean AUC of the Tres model across six datasets analyzed in Fig. 2c is  $0.855 \pm 0.098$ , which is higher than that for TMB and PD-L1 reported in the literature. However, such comparison is limited by the small number of T cell transcriptomic datasets and indirect comparisons across different studies.

**FIBP is a top negative marker of T cell antitumor efficacy.** Encouraged by the performance of Tres in predicting T cell effectiveness, we set out to identify candidate gene regulators and therapeutic targets from Tres signatures. We prioritized genes whose expression levels are consistently associated with worse T cell tumor resilience and poor immunotherapy response in solid tumors. Our analyses focused on negative markers of T cell effectiveness because therapeutic approaches, whether by compounds, antibodies, or genome editing, primarily inhibit target genes.

Among all human genes, *FIBP* ranks first as a negative marker of T cell effectiveness (Fig. 3a and Extended Data Fig. 5a). To the best of our knowledge, very little literature exists for *FIBP* except that *FIBP* may bind FGF1 (ref. <sup>51</sup>) and that *FIBP* enhances chemotherapy resistance in colorectal cancer cell lines<sup>52</sup>. Tres scores of *FIBP* are consistently negative across single-cell datasets (Fig. 1d). *FIBP* expression levels are significantly lower in T cells from anti-PD-1 responders than values from non-responders in solid tumors (Fig. 3a,b and Supplementary Table 6a). Among tumor samples obtained before expanding TILs for adoptive transfer<sup>16</sup>, a high *FIBP* expression level indicates a worse overall survival outcome after adoptive TIL therapy (Fig. 3c and Supplementary Tables 6b and 7). Also, high *FIBP* expression in bulk-tumor transcriptomic data correlates with T cell dysfunction (Fig. 3d, Extended Data Fig. 5b and Supplementary Table 6b).

Tres and other signatures analyzed above are designed to reveal marker genes of T cell antitumor efficacy. Gene markers reflect associations, which may arise from indirect effects rather than causality. Establishing the mechanism of regulatory causality is desirable for the development of therapeutic applications. Therefore, we sought to characterize the effect of Tres marker gene knockouts (KOs) in modulating tumor killing by T cells.

**Antitumor efficacy of *FIBP* KO T cells.** We asked whether knocking out top marker genes identified in Fig. 3a could enhance the antitumor efficacy of T cells. We co-cultured mouse Pmel-1 T cells recognizing the gp100 antigen expressed by the B16-mhgp100 cell line<sup>53</sup>. We knocked out top marker genes (*Fibp*, *Myl12b*, *Psme2*, *Aip*, *Cdk2ap2*, *Park7*, *Prdx2*, *Psmb10* and *Psmb9*; Fig. 3a) in Pmel-1 CD8<sup>+</sup>T cells through the nucleofection of CRISPR Cas9 ribonuclease protein. Among these top markers, only *Fibp* KO consistently promoted T cell-mediated cancer killing compared to controls (Extended Data Fig. 5c), corroborating the top rank of *FIBP* as a negative marker of T cell antitumor efficacy (Extended Data Fig. 5a). We note that the lack of KO phenotypes from other highly ranked genes is not an indication of inaccuracy from Tres. Tres aims to identify marker genes of tumor-resilient T cells, which would not necessarily be expected to result in direct genetic effects when perturbed.

We further examined the *FIBP* KO phenotype in both human and mouse systems (Fig. 4a). For humans, we used NY-ESO-1<sup>+</sup> melanoma cells (A375 and Mel624) as the target of NY-ESO-1 TCR T cells<sup>54</sup>. For mice, we used the gp100 + B16-mhgp100 cell line and the corresponding Pmel-1 TCR T cells<sup>53</sup>. Our target gene was *FIBP*, with *CBLB* as the positive control and *AAVS1* (humans) or *Rosa26* (mice) as the negative controls<sup>55</sup> for CRISPR KOs (Fig. 4b). Previous genome-wide CRISPR screens on T cell proliferation<sup>12</sup> and IL-2 production<sup>13</sup> revealed *CBLB* as the most significant hit (Extended Data Fig. 5d). We utilized the Incucyte imaging system to evaluate

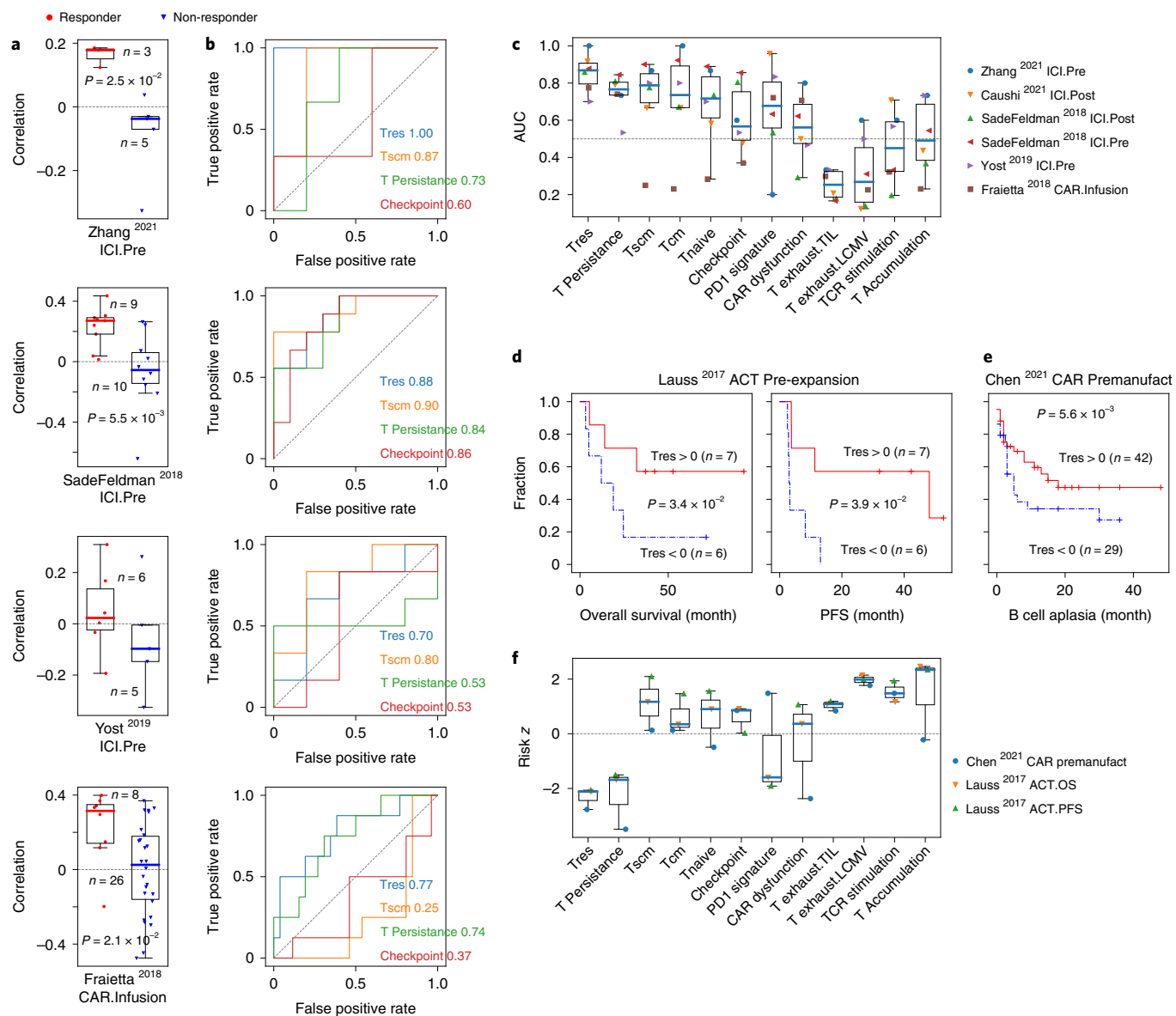


**Fig. 2 | Tres predicts clinical efficacies of ICIs and adoptive cell therapies.** **a**, Tres score correlations predict the efficacy of T cells in immunotherapies. Each data point represents a tumor, with sample counts around each box and cohort names under each panel. The y axis presents the correlation between the Tres signature and the T cell expression profile.  $P$  values were computed through the two-sided Wilcoxon rank-sum test, comparing responders and non-responders. The thick line represents the median value. The bottom and top of the boxes are the 25th and 75th percentiles, respectively (interquartile range). Whiskers encompass 1.5 times the interquartile range. **b**, Tres prediction performance on T cell clinical efficacy. The ROC curve presents false-positive rates against true-positive rates of predicting responders versus non-responders based on signature correlations. The performance of Tres and other signatures was compared to that for random expectations, shown as diagonal lines. **c**, Comparison among T cell signatures in predicting clinical response. The ROC AUC is shown for T cell signatures in Supplementary Table 3, with 0.5 as the random expectation. All box plots have the same format as in **a** ( $n=6$  independent datasets per box). **d**, Tres score correlations in tumors for lymphocyte expansion predict ACT outcome. This plot only included tumors with cytotoxic lymphocyte infiltration higher than average in a melanoma study<sup>46</sup>. The y axis presents the fraction of patients with overall or progression-free survival (PFS) higher than each duration (x axis) for tumors whose transcriptomic profiles have positive or negative correlations with the Tres signature.  $P$  values were evaluated by the two-sided Wald test in the Cox proportional hazards regression without any cutoffs. **e**, Tres correlations in T cells for CAR-T manufacture predict a favorable response. The B cell aplasia duration upon anti-CD19 CAR therapy<sup>48</sup> was shown for patients whose pre-manufacture T cells have positive or negative correlations with the Tres signature as shown in **d**. **f**, Comparison among T cell signatures in predicting survival outcome. For datasets in **d** and **e** ( $n=3$ ), the risk z scores were compared to box plots with the same format as in **a** for T cell signatures in Supplementary Table 3, with zero as the random expectation.

the cancer killing efficacy of T cells co-cultured with tumor cells labeled with tdTomato (Fig. 4c and Methods).

T cells with control KO have cancer-killing efficacy similar to parental T cells for human and mouse donors (Extended Data Fig. 6a,b). In contrast, both human and mouse T cells with *FIBP*

knocked out kill cancer cells at a higher efficacy than control KOs (Fig. 4c–e). Moreover, *FIBP* KOs enhance the release of T cell effector cytokines, including IFN- $\gamma$  and TNF in both human and mouse primary T cells (Fig. 4f). Overall, *FIBP* KO has effects similar in amplitude to the positive control, *CBLB* KO (Fig. 4d–f). Consistent

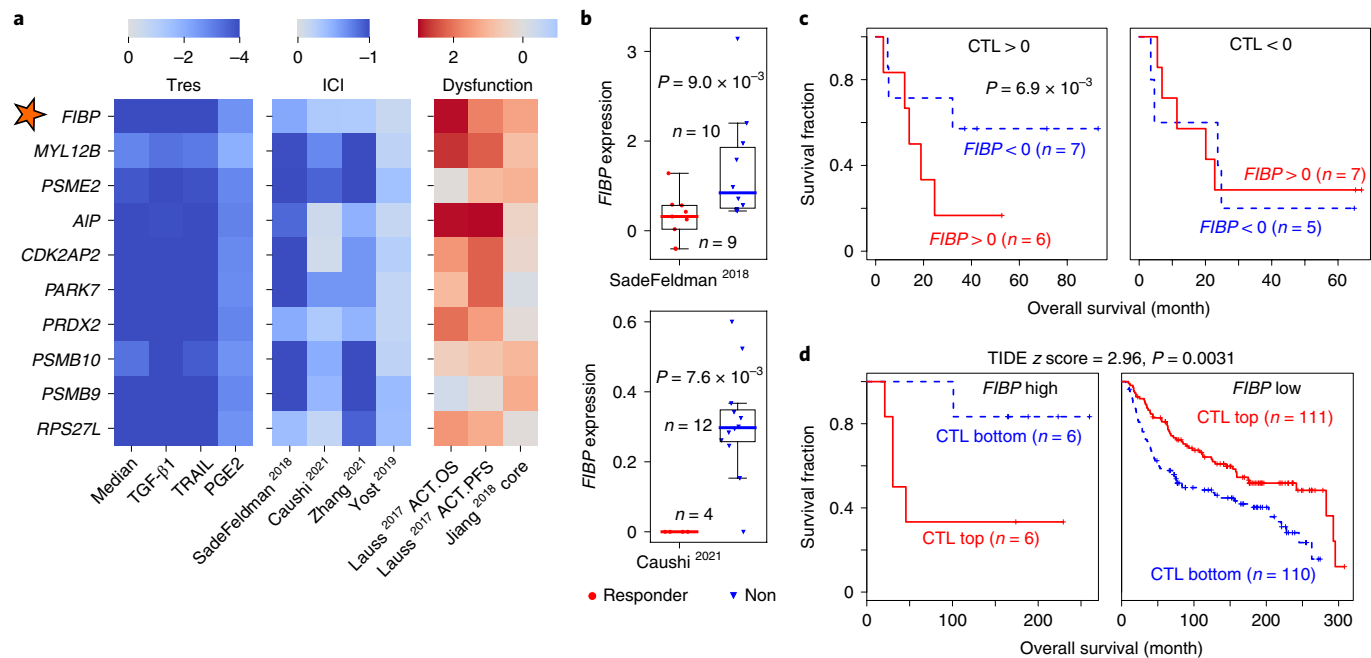


**Fig. 3 | High *FIBP* expression in T cells is associated with inferior clinical efficacy.** **a**, Top ten genes ranked by average signature scores. The first group comprises Tres score computed for different immunosuppressive signals and the median profile among all signals. The second group comprises  $\log_2$  fold change (logFC) of expression values between T cells with high and low efficacies of ICI treatments in solid tumors (Supplementary Table 6a). The third group comprises scores computed under a T cell dysfunction model<sup>68</sup> for bulk tumors (Supplementary Table 6b). **b**, *FIBP* expression in CD8<sup>+</sup>T cells from ICI responders and non-responders. Each dot represents a tumor, with its average value among all T cells on the y axis. The P value was from the two-sided Wilcoxon rank-sum test, comparing group differences. The thick line represents the median value. The bottom and top of the boxes are the 25th and 75th percentiles, respectively (interquartile range). Whiskers encompass 1.5 times the interquartile range. **c**, High *FIBP* expression in tumors for lymphocyte expansion indicates low ACT efficacy. Overall patient survival was shown for tumors with different levels of cytotoxic T lymphocytes (CTLs; median expression of *CD8A*, *CD8B*, *GZMA*, *GZMB* and *PRF1*) and *FIBP* expression. The interaction significance between *FIBP* and CTL on the survival outcome was evaluated by the two-sided interaction test without any cutoffs (Supplementary Table 7). **d**, High *FIBP* levels in bulk tumors indicate T cell dysfunction, generated from the TIDE server<sup>68</sup>. For TNBC tumors<sup>69</sup>, each Kaplan-Meier plot presents tumors in two groups: ‘CTL top’ has above-median CTL values among all samples, whereas ‘CTL bottom’ has values below the median. Samples were split according to the *FIBP* expression level through the best separation criterion maximizing the difference of CTL-survival associations between two groups. TIDE scores and P values were computed through the two-sided interaction test using continuous values without any cutoffs.

with these results, *FIBP* KO CD8<sup>+</sup>T cells had enhanced proliferation (Extended Data Fig. 6c–e) and early-activated fractions (Extended Data Fig. 6f).

**In vivo antitumor efficacies of *Fibp* KO T cells.** We next evaluated whether knocking out *FIBP* could enhance the in vivo efficacy of transferred Pmel-1 T cells (Fig. 5a and Methods). We randomized C57BL/6 mice into five different treatment groups: *Fibp* KO ( $n=15$ ), *Rosa26* KO (negative control,  $n=15$ ), *Cblb* KO (positive control,  $n=15$ ), wild-type T cells ( $n=5$ ) and no-treatment control (saline injection,  $n=5$ ) (Extended Data Fig. 7a,b). Compared to no-treatment controls, wild-type T cell adoptive transfer significantly repressed the growth of gp100<sup>+</sup> tumors and *Rosa26* KO T cells did not have lower antitumor efficacy than parental T cells (Extended Data Fig. 7c,d).

Compared to *Rosa26* KO T cells, *Fibp* KO T cells significantly reduced tumor size (Fig. 5b–d). The overall tumor size reduction effect of *Fibp* KO T cells was comparable to the positive control *Cblb* KO T cells before any mice reached end points (Fig. 5c,d). Both *Fibp* and *Cblb* KO T cell recipients had significantly longer survival than *Rosa26* KO T cell recipients (Fig. 5e; one-sided log-rank P value = 0.04 and 0.016 for *Fibp* and *Cblb*, respectively). These results support *Fibp* KO as a potential therapeutic approach to enhance adoptive T cell therapy.

To analyze the in vivo phenotype of T cells, we performed multidimensional flow analyses on CD8<sup>+</sup>T cells isolated from mouse

tumors at early time points after adoptive cell transfer. *Fibp* KO T cells had a higher CD69<sup>+</sup> fraction than *Rosa26* KO T cells (Fig. 5f), whereas other memory/effector or exhaustion markers were not significantly different (Extended Data Fig. 7e,f). Similarly, in a previous in vitro analysis, both human and mouse donor *FIBP* KO T cells had higher CD69<sup>+</sup> fractions than control KO T cells (Extended Data Fig. 6f). The high fraction of CD69<sup>+</sup>T cells suggests increased activation of T cells upon *Fibp* KO. Meanwhile, our data suggest that *FIBP* does not impact memory or effector T cell differentiation or promote exhaustion, but we would not expect the T cell antitumor efficacy to necessarily be tied to these cell states.

***FIBP* KO limits cholesterol metabolism in T cells.** To gain mechanistic insights into *FIBP*'s inhibitory effects on T cells, we performed RNA-seq in murine Pmel-1 *Fibp* KO versus *Rosa26* KO T cells (Fig. 6a). Ingenuity Pathway Analysis (IPA) revealed that all top enrichments upon *Fibp* KO are related to the downregulation of cholesterol metabolism (Fig. 6b). Compared to *Rosa26* KOs, *Fibp* KOs had downregulated expression of multiple cholesterol biosynthesis enzymes, such as *Hmgcs* and *Sqle* and the cell-surface receptor *Ldlr*, modulating cholesterol intake and upregulated expression of the cholesterol efflux pump *Abca1* (ref. 56) (Fig. 6c).

To further investigate associations between *FIBP* and cholesterol metabolism, we analyzed the correlation between *FIBP* and

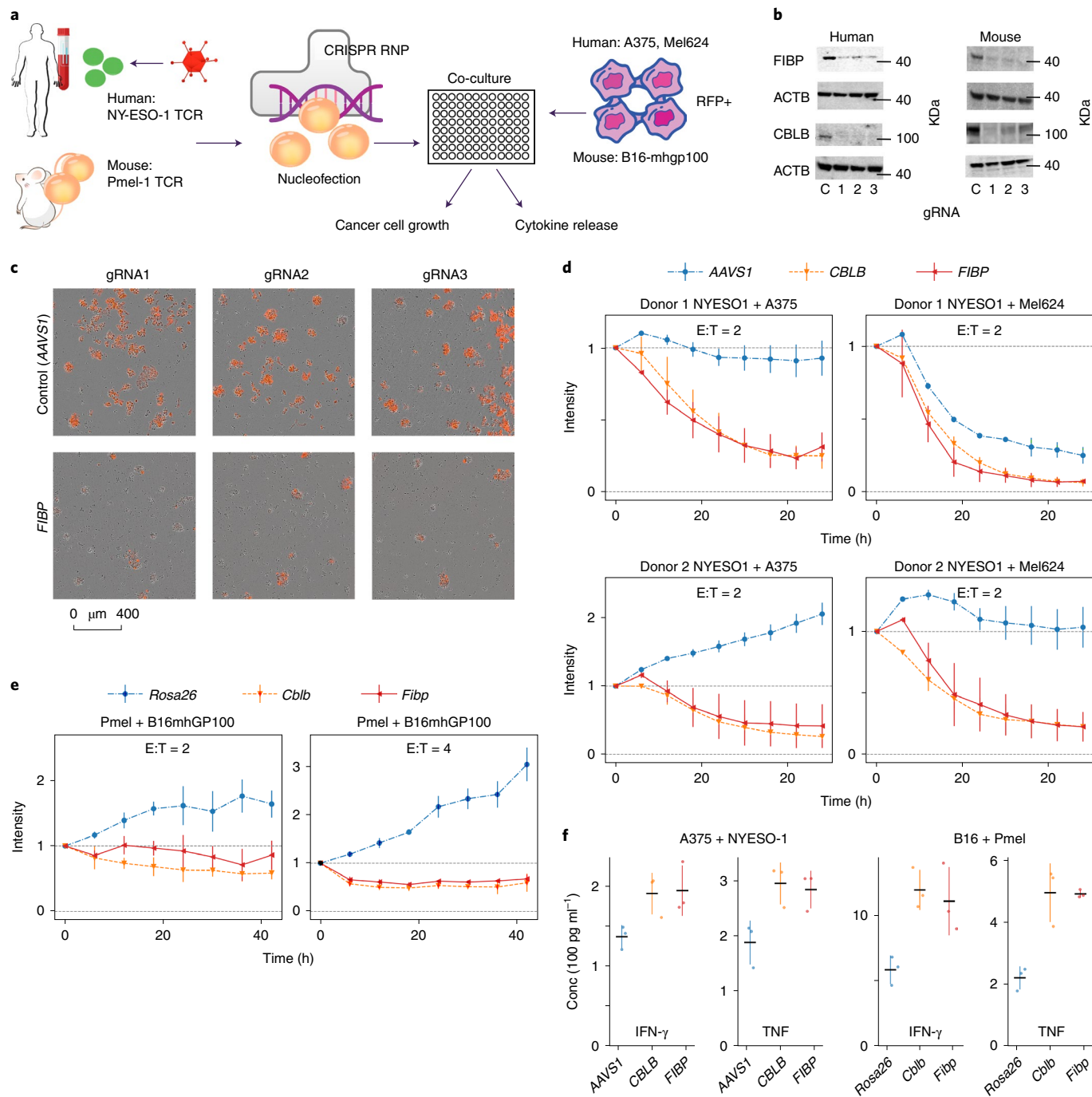


**Fig. 4 | FIBP knockout CD8<sup>+</sup> T cells exhibit enhanced cytotoxicity.** **a**, Co-culture between CD8<sup>+</sup> T cells and cancer cells. The readout is cancer cell killing measured by the Incucyte and cytokine release measured by ELISA. **b**, Western blots of CRISPR KO efficiency. For each protein with antibodies available, the protein levels in T cells from human donor 1 and Pmel-1 transgenic mice were shown for control (C; AAVS1 for human and Rosa26 for mice) and three independent gRNAs (raw images in Supplementary Fig. 1). **c**, Image-based co-culture killing assay. In this example, human T cells from donor no. 1 targeting NY-ESO-1 antigen were incubated with A375 cells at an effector-to-tumor (E:T) ratio of two. The red fluorescent protein (RFP) intensity of cancer cells was measured using the Incucyte at 48 h for both AAVS1 control and *FIBP* KOs with three independent gRNAs (raw images in Supplementary Fig. 2). **d**, *FIBP* KOs in human donor T cells enhanced the cancer-killing efficacy. The killing efficacy of T cells from two donors targeting the NY-ESO-1 antigen was evaluated with A375 and Mel624 cell lines at an E:T ratio of two as described in **c**. The T cell efficacy, measured as the relative RFP intensity (y axis) from time zero, was compared across various gene KOs at different time points (x axis). Each data point is the median value among three independent gRNAs with s.d. shown as error bars. **e**, *Fibp* KOs in mouse Pmel-1 T cells enhanced its killing efficacy on B16-mhgp100 cells. The efficacy of T cell-mediated cancer killing was shown for murine cells with two E:T ratios as for **d**. Mean values were computed through three independent gRNAs with s.d. shown as error bars. **f**, *FIBP* KOs in T cells enhanced the release of T cell effector cytokines. The IFN- $\gamma$  and TNF cytokine concentrations were measured for different gene KOs by the ELISA assay. The mean and s.d. are shown ( $n=3$  independent gRNAs). The comparison between gene KO and control conditions was performed using a two-sided Wilcoxon rank-sum test ( $P=0.05$  for all comparisons).

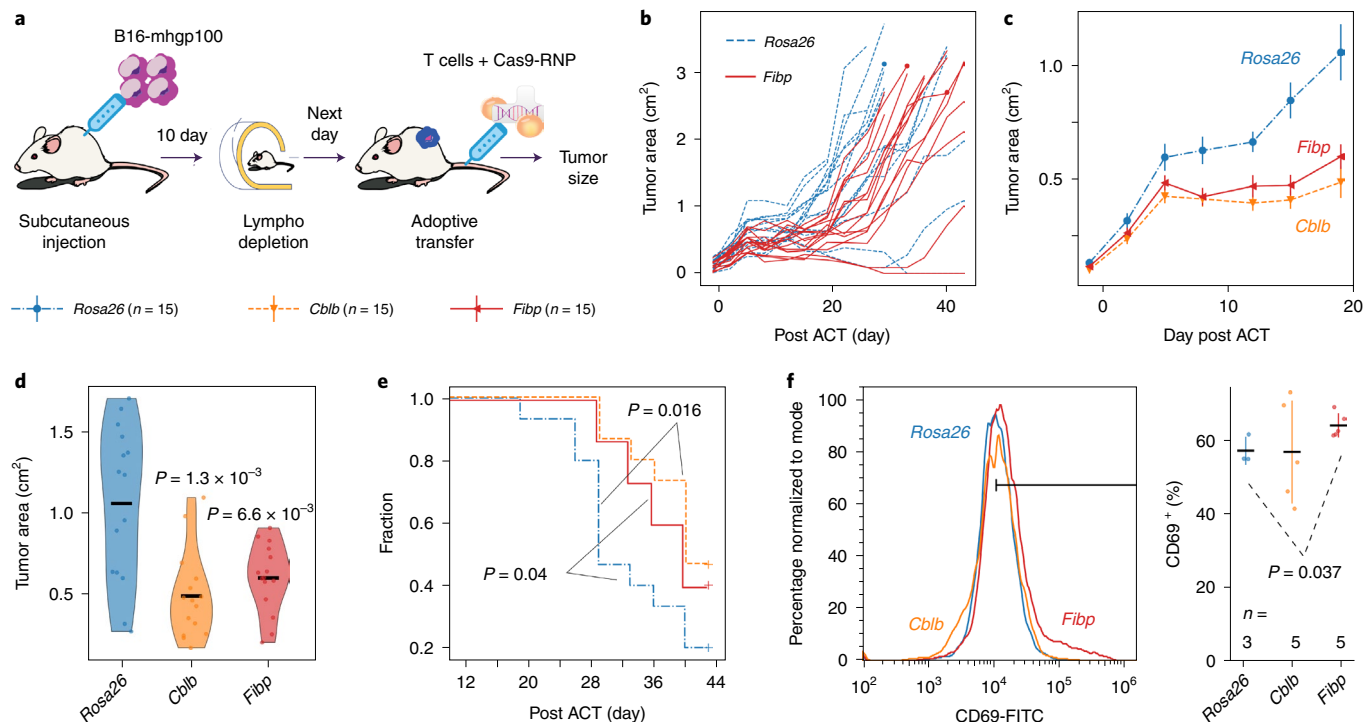


**Fig. 5 | Adoptively transferred *FIBP* KO T cells exhibit enhanced in vivo efficacy in the B16 tumor model.** **a**, Adoptive T cell transfer procedure. The B16-mhgp100 cell line was implanted in C57BL/6 mice. Lymphodepletion through radiation was performed 10 d after tumor injection and T cells with different gene KOs were injected the day after. Tumor size measurements were taken twice a week in a double-blind manner. **b**, Tumor growth curves in mice treated with T cells with *Fibp* and *Rosa26* KOs. The tumor area (length × width) was measured after ACT ( $n=15$  mice per group). **c**, Average tumor size in mice treated with T cells with gene KOs. The tumor area mean was shown when no mice had reached end points (long dimension >20 mm or death). Error bars indicate s.e.m. ( $n=15$  mice per group). **d**, Tumor size at the last time point at which no mice had reached the end point. All tumor size distributions at day 19 were shown through violin plots smoothed by a kernel density estimator ( $n=15$  mice per group). The comparison between each target group and the *Rosa26* control was performed using a two-sided Wilcoxon rank-sum test. **e**, Kaplan-Meier curves of event-free survival. For each group ( $n=15$  mice), the fraction of mice that did not reach the end point (long dimension >20 mm or death) was shown at different days after ACT. The survival comparison between the target group and *Rosa26* control was conducted using a one-sided log-rank test. **f**, In vivo flow analysis of CD69 T cell activation marker. Representative histograms for gene KO T cells isolated from mouse tumors (left). Mean and s.d. are shown as error bars (tumor counts labeled under each group, growth curves in Supplementary Fig. 3) (right). Different KOs were compared using a one-sided Wilcoxon rank-sum test. Only significant  $P$  values are shown.

cholesterol pathway genes across leukemia clinical samples from the MILE project, in which cancer cells have a hematopoietic lineage related to T cells<sup>57</sup>. *FIBP* expression is positively correlated with positive regulators of cholesterol metabolism and negatively correlated with negative regulators (Extended Data Fig. 8a,b). Further, we used public chromatin immunoprecipitation (ChIP)-seq data<sup>58</sup> to identify target genes of SREBF2, the master transcription factor promoting cholesterol metabolism<sup>59</sup> and found SREBF2 targets to be significantly downregulated upon *Fibp* KO (Extended Data Fig. 8c and Supplementary Table 8).

We validated the altered expression of several identified cholesterol pathway genes (*ABCA1*, *LDLR* and *SREBF2*) and cholesterol synthesis enzymes using quantitative PCR with reverse transcription (RT-qPCR) on both mouse and human *FIBP* KO T cells (Fig. 6d and Extended Data Fig. 8d). We also confirmed decreases in expression of *LDLR* protein and *SREBF2* protein (both inactivated full-length and NH2-cleaved activated forms<sup>59</sup>) by western blotting of *Fibp* KO cells (Fig. 6e). Conversely, *Fibp* overexpression in T cells led to increased expression of cholesterol metabolism regulators at both the mRNA and protein levels (Fig. 6f and Extended Data Fig. 8e). Consistent with these results, both in vivo (T cells extracted from mouse tumors post-adoptive transfer) and in vitro cholesterol levels in *Fibp* KO T cells were significantly lower than levels in *Rosa26* KO T cells (Fig. 6g and Extended Data Fig. 9a-d). Also, the

cholesterol level in T cells increased significantly upon *Fibp* overexpression (Fig. 6h and Extended Data Fig. 9d).

We did not observe a cholesterol level change in *Cblb* KO T cells (Fig. 6g and Extended Data Fig. 9b). Previous studies demonstrated that *CBLB* inhibition enhanced T cell antitumor efficacy by promoting IL-2 production and autocrine signaling<sup>60</sup>. However, *FIBP* KO does not alter IL-2 production in T cells<sup>13</sup> (Extended Data Fig. 5d, right). These data suggest that inhibiting different gene targets may promote T cell antitumor efficacy through orthogonal mechanisms.

**Inhibition of T cell functions by cholesterol relies on *FIBP*.** Previous studies have revealed the effects of cholesterol on the antitumor activity of T cells through inhibiting effector T cell functions<sup>61</sup> and inducing T cell exhaustion<sup>62</sup>. Similarly, our co-culture assay shows that cholesterol treatment of T cells significantly inhibited cancer-killing efficacy (Fig. 6i, left). However, *Fibp* KO T cells retain their cancer-killing efficacy even after cholesterol treatment (Fig. 6i, right).

Previous studies have also demonstrated that low-density lipoprotein (LDL) uptake compromises the antitumor function of T cells<sup>63</sup>. *Fibp* KO resulted in a marked reduction of LDL uptake after lipoprotein starvation (Extended Data Fig. 9e). These results show that *Fibp* KO, through downregulation of cholesterol biosynthesis and transport, renders CD8<sup>+</sup> T cells resistant to the

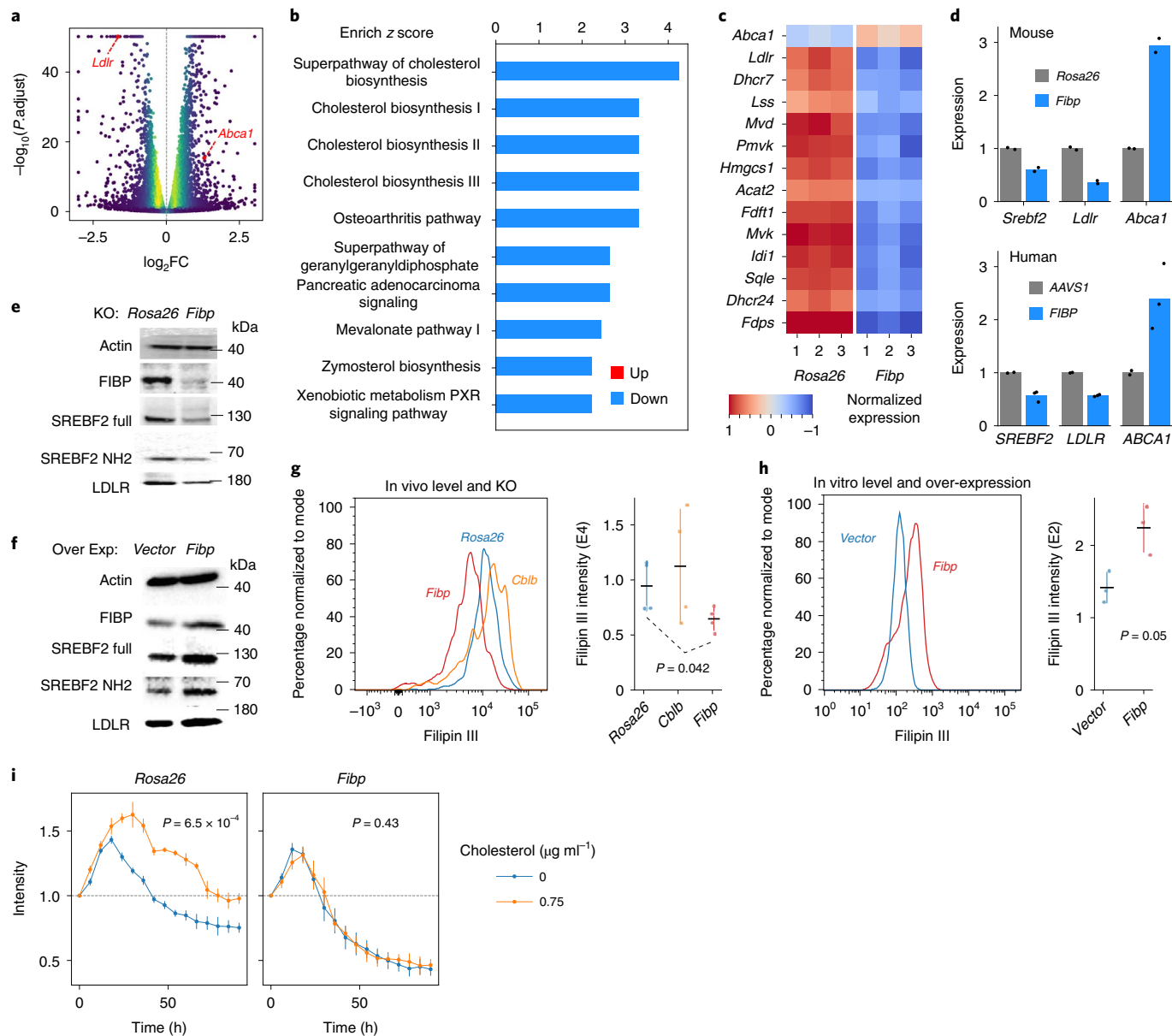


**Fig. 6 | *FIBP* KO inhibits cholesterol metabolism to enhance T cell antitumor efficacy.** **a**, Differential gene expression in T cells upon *Fibp* KO. Each dot represents one gene ( $n=14,537$ ). The  $\log_2$ FC and DESeq2 adjusted  $P$  values were computed by comparing RNA-seq counts between *Fibp* and Rosa26 control KOs. **b**, Pathway enrichments in *Fibp* KO expression profiles, from the IPA for up- and downregulated pathways. **c**, Expression values of genes in cholesterol metabolism. We only included genes with  $|\log_2\text{FC}| > 1$ . All gene values were normalized by mean and s.d. across all profiles ( $n=3$  independent gRNAs). **d**, RT-qPCR validation of essential genes in cholesterol metabolism. Normalized expression levels were shown for control (Rosa26 for mouse and AAVS1 for human) and *FIBP* KOs, with mean from two independent gRNAs. **e**, Western blots of cholesterol metabolism regulators after *Fibp* KO. Protein levels of SREBF2 (inactivated full-length and activated N-terminal NH2 fragments), LDLR and actin control were shown for Rosa26 control and *Fibp* KOs in mouse T cells (raw images are shown in Supplementary Fig. 4). **f**, Western blots of cholesterol metabolism regulators after *Fibp* overexpression. Protein levels are shown as in **e** for vector control and *Fibp* overexpression in mouse T cells (raw images are shown in Supplementary Fig. 5). **g**, In vivo flow analysis of cholesterol levels (Filipin III) in gene KO T cells isolated from mouse tumors (left). Mean and s.d. are shown as error bars ( $n=4$  tumors per group) (right). Different KOs were compared using a one-sided Wilcoxon rank-sum test. **h**, In vitro cholesterol levels in T cells with overexpression of *Fibp* and control vectors as shown in **g**. The group difference was compared using a two-sided Wilcoxon rank-sum test ( $n=3$  cell culture replicates per condition). **i**, A high-cholesterol environment inhibits T cell cytotoxicity. The killing efficacy on B16-mhgp100 cells was shown for T cells with Rosa26 control and *Fibp* KOs in a regular and high-cholesterol medium, with mean and s.e.m. shown as error bars ( $n=6$  cell culture replicates).  $P$  values were obtained using a two-sided Wilcoxon signed-rank test, comparing the high-cholesterol and control groups.

immunosuppressive effects of high cholesterol levels, a common feature of the tumor microenvironment<sup>62</sup>.

A potential alternative anti-cholesterol treatment is statin, a widely used drug that lowers cholesterol synthesis. Of note, we observed that statin reduced cholesterol levels in T cells only before

activation (Extended Data Fig. 10a). After activation, simvastatin treatment elevated cholesterol levels in T cells (Extended Data Fig. 10b). Also, statin treatment inhibited T cell proliferation (Extended Data Fig. 10c,d), consistent with previous studies showing that statin inhibits T cell activation and proliferation<sup>64</sup>.

These results suggest opposite effects between statin treatment and *FIBP* KO in effector T cells; statin treatment elevates cholesterol levels and reduces T cell proliferation, whereas *FIBP* KO inhibits cholesterol metabolism and promotes antitumor T cell responses.

## Discussion

We developed a Tres model to identify transcriptomic signatures of T cells that are resilient to immunosuppressive signals in solid tumors. The Tres signature can reliably predict the T cell efficacy in immune-checkpoint blockade and adoptive cell therapy (ACT) using training data from tumors without any accompanying immunotherapies. This advantage is significant as most single-cell studies do not have immunotherapy outcome information. Tres can repurpose single-cell data from diverse cancer types to develop pre-treatment biomarkers.

A few limitations of Tres should be noted. When training Tres scores, 38 out of 168 tumors did not achieve statistical significance (Supplementary Table 1). Potential reasons include insufficient data quality, absence of tumor-resilient T cells in a tumor or alternative immunosuppressive signals not modeled by Tres. The interaction test utilized by Tres assumes that regression variables, such as immunosuppression and T cell proliferation, should have sufficient variations<sup>65</sup>. Therefore, the Tres model will not give meaningful results in highly immunosuppressive tumors, where all T cells are deeply dysfunctional without any variances, leading the covariate matrix in regression close to singular<sup>65</sup>.

Our analysis revealed *FIBP* as a negative marker of tumor-resilient T cells in solid tumors, with mechanistic studies showing that *FIBP* KO enhances T cell antitumor efficacy through downregulation of cholesterol metabolism. Previous studies<sup>62</sup>, together with our results, indicate the promise of combining immunotherapies with anti-cholesterol therapies. A seemingly contradictory result from previous studies is that cholesterol is essential for naive T cell activation<sup>66</sup>; however, experiments in the current study were performed in activated effector T cells, but not in naive T cells. Also, *FIBP* KO reduces but does not fully abrogate cholesterol biosynthesis in T cells.

Little is known about the molecular function of *FIBP*. We could not identify any DNA or protein-binding domains in the *FIBP* protein sequence<sup>67</sup>. *FIBP* has been reported to be an intracellular protein that binds to the acidic fibroblast growth factor<sup>51</sup> and to be an oncogene that induces chemotherapy resistance in colorectal cancer cells<sup>52</sup>. The growth-inhibitory effect of *FIBP* knockdown in cancer cells<sup>52</sup>, in contrast to the efficacy-promoting effect of *FIBP* KO in CD8<sup>+</sup>T cells, suggests that *FIBP* may regulate distinct cellular programs in a lineage-dependent way. Also, these results together indicate that *FIBP* inhibitors may exert antitumor effects in both cancer and T cells.

While *FIBP* KO in adoptive T cell transfer is feasible, it is unclear whether it is possible to design pharmacological inhibitors of *FIBP*. Also, our study did not evaluate whether *FIBP* KO T cells can synergize with ICIs and other treatments, such as targeted therapies, chemotherapy or radiotherapy. Therefore, more data are needed to support the viability of *FIBP* as a therapeutic target.

Our data-driven strategy provides proof of concept for identifying signatures of tumor-resilient T cells. We foresee Tres being used by basic researchers to identify new targets in T cells in pursuit of next-generation cell therapies, by clinical researchers to identify immunotherapy response biomarkers for routine clinical use and directly by clinicians to predict cell therapy response from pre-manufacture samples or infusion products.

## Online content

Any methods, additional references, Nature Research reporting summaries, source data, extended data, supplementary information, acknowledgements, peer review information; details of

author contributions and competing interests; and statements of data and code availability are available at <https://doi.org/10.1038/s41591-022-01799-y>.

Received: 30 June 2021; Accepted: 24 March 2022;  
Published online: 2 May 2022

## References

- Ribas, A. & Wolchok, J. D. Cancer immunotherapy using checkpoint blockade. *Science* <https://doi.org/10.1126/science.aar4060> (2018).
- Rosenberg, S. A. et al. Durable complete responses in heavily pretreated patients with metastatic melanoma using T-cell transfer immunotherapy. *Clin. Cancer Res.* <https://doi.org/10.1158/1078-0432.CCR-11-0116> (2011).
- Robbins, P. F. et al. Tumor regression in patients with metastatic synovial cell sarcoma and melanoma using genetically engineered lymphocytes reactive with NY-ESO-1. *J. Clin. Oncol.* <https://doi.org/10.1200/JCO.2010.32.2537> (2011).
- Guedan, S., Ruella, M. & June, C. H. Emerging cellular therapies for cancer. *Annu. Rev. Immunol.* <https://doi.org/10.1146/annurev-immunol-042718-041407> (2019).
- Martinez, M. & Moon, E. K. CAR T cells for solid tumors: new strategies for finding, infiltrating, and surviving in the tumor microenvironment. *Front. Immunol.* <https://doi.org/10.3389/fimmu.2019.00128> (2019).
- Sharma, P., Hu-Lieskovian, S., Wargo, J. A. & Ribas, A. Primary, adaptive, and acquired resistance to cancer immunotherapy. *Cell* **168**, 707–723 (2017).
- Tschumi, B. O. et al. CART cells are prone to Fas- and DR5-mediated cell death. *J. Immunother. Cancer* **6**, 71 (2018).
- Green, D. R., Droin, N. & Piskoski, M. Activation-induced cell death in T cells. *Immunol. Rev.* <https://doi.org/10.1034/j.1600-065x.2003.00051.x> (2003).
- Sade-Feldman, M. et al. Defining T cell states associated with response to checkpoint immunotherapy in melanoma. *Cell* **175**, 998–1013 (2018).
- Caushi, J. X. et al. Transcriptional programs of neoantigen-specific TIL in anti-PD-1-treated lung cancers. *Nature* **596**, 126–132 (2021).
- Suvà, M. L. & Tirosh, I. Single-cell RNA sequencing in cancer: lessons learned and emerging challenges. *Mol. Cell* **75**, 7–12 (2019).
- Shifrut, E. et al. Genome-wide CRISPR screens in primary human T cells reveal key regulators of immune function. *Cell*. <https://doi.org/10.1016/j.cell.2018.10.024> (2018).
- Schmidt, R. et al. CRISPR activation and interference screens decode stimulation responses in primary human T cells. *Science*. <https://doi.org/10.1126/science.abj4008> (2022).
- Legut, M. et al. A genome-scale screen for synthetic drivers of T cell proliferation. *Nature*. <https://doi.org/10.1038/s41586-022-04494-7> (2022).
- Zhou, P. et al. In vivo discovery of immunotherapy targets in the tumour microenvironment. *Nature* **506**, 52–57 (2014).
- Dong, M. B. et al. Systematic immunotherapy target discovery using genome-scale in vivo CRISPR screens in CD8 T cells. *Cell* **178**, 1189–1204 (2019).
- Gicobi, J. K., Barham, W. & Dong, H. Immune resilience in response to cancer therapy. *Cancer Immunol. Immunother.* **69**, 2165–2167 (2020).
- Jerby-Arnon, L. et al. A cancer cell program promotes T cell exclusion and resistance to checkpoint blockade. *Cell* **175**, 984–997 (2018).
- Jiang, P. et al. Systematic investigation of cytokine signaling activity at the tissue and single-cell levels. *Nat. Methods* **18**, 1181–1191 (2021).
- Kanehisa, M., Sato, Y., Kawashima, M., Furumichi, M. & Tanabe, M. KEGG as a reference resource for gene and protein annotation. *Nucleic Acids Res.* **44**, D457–D462 (2016).
- Wehbi, V. L. & Taskén, K. Molecular mechanisms for cAMP-mediated immunoregulation in T cells – role of anchored protein kinase A signaling units. *Front. Immunol.* <https://doi.org/10.3389/fimmu.2016.00222> (2016).
- Naing, A. et al. PEGylated IL-10 (pegilodecakin) induces systemic immune activation, CD8 T cell invigoration and polyclonal T cell expansion in cancer patients. *Cancer Cell* **34**, 775–791 (2018).
- Santra, S. & Ghosh, S. K. Interleukin-4 is effective in restoring cytotoxic T cell activity that declines during in vivo progression of a murine B lymphoma. *Cancer Immunol. Immunother.* <https://doi.org/10.1007/s00260050385> (1997).
- Krishna, S. et al. Stem-like CD8 T cells mediate response of adoptive cell immunotherapy against human cancer. *Science* **370**, 1328–1334 (2020).
- Subramanian, A. et al. Gene set enrichment analysis: a knowledge-based approach for interpreting genome-wide expression profiles. *Proc. Natl Acad. Sci. USA* **102**, 15545–15550 (2005).
- Lee, N. et al. HLA-E is a major ligand for the natural killer inhibitory receptor CD94/NKG2A. *Proc. Natl Acad. Sci. USA* **95**, 5199–5204 (1998).
- Lu, L. et al. Regulation of activated CD4<sup>+</sup> T cells by NK cells via the Qa-1-NKG2A inhibitory pathway. *Immunity* **26**, 593–604 (2007).
- Soderquest, K. et al. Cutting edge: CD8<sup>+</sup> T cell priming in the absence of NK cells leads to enhanced memory responses. *J. Immunol.* **186**, 3304–3308 (2011).

29. Azizi, E. et al. Single-cell map of diverse immune phenotypes in the breast tumor microenvironment. *Cell*. <https://doi.org/10.1016/j.cell.2018.05.060> (2018).
30. Wu, S. Z. et al. A single-cell and spatially resolved atlas of human breast cancers. *Nat. Genet.* <https://doi.org/10.1038/s41588-021-00911-1> (2021).
31. Steen, C. B. et al. The landscape of tumor cell states and ecosystems in diffuse large B cell lymphoma. *Cancer Cell*. <https://doi.org/10.1016/j.ccr.2021.08.011> (2021).
32. Mathewson, N. D. et al. Inhibitory CD161 receptor identified in glioma-infiltrating T cells by single-cell analysis. *Cell*. <https://doi.org/10.1016/j.cell.2021.01.022> (2021).
33. Puram, S. V. et al. Single-cell transcriptomic analysis of primary and metastatic tumor ecosystems in head and neck cancer. *Cell*. <https://doi.org/10.1016/j.cell.2017.10.044> (2017).
34. Ma, L. et al. Tumor cell biodiversity drives microenvironmental reprogramming in liver cancer. *Cancer Cell*. <https://doi.org/10.1016/j.ccr.2019.08.007> (2019).
35. Liu, Y. et al. Tumour heterogeneity and intercellular networks of nasopharyngeal carcinoma at single cell resolution. *Nat. Commun.* <https://doi.org/10.1038/s41467-021-21043-4> (2021).
36. Lambrechts, D. et al. Phenotype molding of stromal cells in the lung tumor microenvironment. *Nat. Med.* **24**, 1277–1289 (2018).
37. Young et al. Single-cell transcriptomes from human kidneys reveal the cellular identity of renal tumors. *Science*. <https://doi.org/10.1126/science.aat1699> (2018).
38. Durante, M. A. et al. Single-cell analysis reveals new evolutionary complexity in uveal melanoma. *Nat. Commun.* <https://doi.org/10.1038/s41467-019-14256-1> (2020).
39. Zheng, L. et al. Pan-cancer single-cell landscape of tumor-infiltrating T cells. *Science*. <https://doi.org/10.1126/science.abe6474> (2021).
40. Zhang, Y. et al. Single-cell analyses reveal key immune cell subsets associated with response to PD-L1 blockade in triple-negative breast cancer. *Cancer Cell*. <https://doi.org/10.1016/j.ccr.2021.09.010> (2021).
41. Yost, K. E. et al. Clonal replacement of tumor-specific T cells following PD-1 blockade. *Nat. Med.* **25**, 1251–1259 (2019).
42. Gattinoni, L. et al. A human memory T cell subset with stem cell-like properties. *Nat. Med.* <https://doi.org/10.1038/nm.2446> (2011).
43. Doering, T. A. et al. Network analysis reveals centrally connected genes and pathways involved in CD8<sup>+</sup> T cell exhaustion versus memory. *Immunity*. <https://doi.org/10.1016/j.jimmuni.2012.08.021> (2012).
44. Good, C. R. et al. An NK-like CAR T cell transition in CAR T cell dysfunction. *Cell*. <https://doi.org/10.1016/j.cell.2021.11.016> (2021).
45. Giordano, M. et al. Molecular profiling of CD8 T cells in autochthonous melanoma identifies Maf as driver of exhaustion. *EMBO J.* **34**, 2042–2058 (2015).
46. Lauss, M. et al. Mutational and putative neoantigen load predict clinical benefit of adoptive T cell therapy in melanoma. *Nat. Commun.* **8**, 1738 (2017).
47. Fraietta, J. A. et al. Determinants of response and resistance to CD19 chimeric antigen receptor (CAR) T cell therapy of chronic lymphocytic leukemia. *Nat. Med.* **24**, 563–571 (2018).
48. Chen, G. M. et al. Integrative bulk and single-cell profiling of premanufacture T-cell populations reveals factors mediating long-term persistence of CAR T-cell therapy. *Cancer Discov.* **11**, 2186–2199 (2021).
49. Lu, S. et al. Comparison of biomarker modalities for predicting response to PD-1/PD-L1 checkpoint blockade: a systematic review and meta-analysis. *JAMA Oncol.* **5**, 1195–1204 (2019).
50. Litchfield, K. et al. Meta-analysis of tumor- and T cell-intrinsic mechanisms of sensitization to checkpoint inhibition. *Cell*. <https://doi.org/10.1016/j.cell.2021.01.002> (2021).
51. Kolpakova, E. et al. Cloning of an intracellular protein that binds selectively to mitogenic acidic fibroblast growth factor. *Biochem. J.* **336**, 213–222 (1998).
52. Huang, Y.-F. et al. FIBP knockdown attenuates growth and enhances chemotherapy in colorectal cancer via regulating GSK3 $\beta$ -related pathways. *Oncogenesis* **7**, 77 (2018).
53. Hanada, K.-I., Yu, Z., Chappell, G. R., Park, A. S. & Restifo, N. P. An effective mouse model for adoptive cancer immunotherapy targeting neoantigens. *JCI Insight*. <https://doi.org/10.1172/jci.insight.124405> (2019).
54. Patel, S. J. et al. Identification of essential genes for cancer immunotherapy. *Nature* **548**, 537–542 (2017).
55. Chu, V. T. et al. Increasing the efficiency of homology-directed repair for CRISPR-Cas9-induced precise gene editing in mammalian cells. *Nat. Biotechnol.* **33**, 543–548 (2015).
56. Luo, J., Yang, H. & Song, B. L. Mechanisms and regulation of cholesterol homeostasis. *Nat. Rev. Mol. Cell Biol.* <https://doi.org/10.1038/s41580-019-0190-7> (2020).
57. Kohlmann, A. et al. An international standardization programme towards the application of gene expression profiling in routine leukaemia diagnostics: the Microarray Innovations in LEukemia study prephase. *Br. J. Haematol.* **142**, 802–807 (2008).
58. Jiang, P., Freedman, M. L., Liu, J. S. & Liu, X. S. Inference of transcriptional regulation in cancers. *Proc. Natl Acad. Sci. USA*. <https://doi.org/10.1073/pnas.1424272112> (2015).
59. Brown, M. S. & Goldstein, J. L. The SREBP pathway: regulation of cholesterol metabolism by proteolysis of a membrane-bound transcription factor. *Cell*. [https://doi.org/10.1016/S0092-8674\(00\)80213-5](https://doi.org/10.1016/S0092-8674(00)80213-5) (1997).
60. Stromnes, I. M. et al. Abrogating Cbl-b in effector CD8<sup>+</sup> T cells improves the efficacy of adoptive therapy of leukemia in mice. *J. Clin. Invest.* **120**, 3722–3734 (2010).
61. Chen, Y. et al. Cholesterol inhibits TCR signaling by directly restricting TCR-CD3 core tunnel motility. *Molecular Cell*. <https://doi.org/10.1016/j.molcel.2022.02.017> (2022).
62. Ma, X. et al. Cholesterol induces CD8 T cell exhaustion in the tumor microenvironment. *Cell Metab.* **30**, 143–156 (2019).
63. Rodrigues, N. V. et al. Low-density lipoprotein uptake inhibits the activation and antitumor functions of human V $\gamma$ 9V $\delta$ 2 T cells. *Cancer Immunol. Res.* **6**, 448–457 (2018).
64. Blank, N. et al. Atorvastatin inhibits T cell activation through 3-hydroxy-3-methylglutaryl coenzyme A reductase without decreasing cholesterol synthesis. *J. Immunol.* **179**, 3613–3621 (2007).
65. James, G., Witten, D., Hastie, T. & Tibshirani, R. *An Introduction to Statistical Learning: with Applications in R* (Springer, 2013).
66. Kidani, Y. et al. Sterol regulatory element-binding proteins are essential for the metabolic programming of effector T cells and adaptive immunity. *Nat. Immunol.* **14**, 489–499 (2013).
67. Marchler-Bauer, A. et al. CDD/SPARCLE: functional classification of proteins via subfamily domain architectures. *Nucleic Acids Res.* **45**, D200–D203 (2017).
68. Jiang, P. et al. Signatures of T cell dysfunction and exclusion predict cancer immunotherapy response. *Nat. Med.* **24**, 1550–1558 (2018).
69. Curtis, C. et al. The genomic and transcriptomic architecture of 2,000 breast tumours reveals novel subgroups. *Nature* **486**, 346–352 (2012).

**Publisher's note** Springer Nature remains neutral with regard to jurisdictional claims in published maps and institutional affiliations.

Springer Nature or its licensor holds exclusive rights to this article under a publishing agreement with the author(s) or other rightsholder(s); author self-archiving of the accepted manuscript version of this article is solely governed by the terms of such publishing agreement and applicable law.

This is a U.S. government work and not under copyright protection in the U.S.; foreign copyright protection may apply 2022, corrected publication 2022

## Methods

This research complies with all relevant ethical regulations, approved by the National Cancer Institute (NCI) Animal Ethics Committee, the Institutional Review Board of the NCI and the Committee of the Use of Live Animals in Teaching and Research at the University of Hong Kong.

**Processing of single-cell RNA-seq data.** For all single-cell datasets, we standardized the transcriptomic levels to  $\log_2(\text{TPM} / 10 + 1)$ . To train Tres signatures, we normalized the expression values of each gene to zero mean across all cells within each dataset. Tres scores were computed for CD8<sup>+</sup>T cells labeled by the original study or all T cells if CD8 was not labeled in the original study (Supplementary Table 1). A total of 411 common stress genes related to enzymatic dissociations used to prepare samples in single-cell studies were removed for all analyses<sup>70</sup>. To validate the Tres prediction performance using single-cell data, we generated the average transcriptomic profiles among all T cells sequenced for each tumor as a bulk profile.

**Selection of immunosuppressive signals.** The first stage in the Tres framework utilized cytokine signaling activities predicted by CytoSig<sup>19</sup>. For 51 cytokines, CytoSig estimates their signaling activities based on target genes modulated upon cytokine treatment collected from public transcriptomics data repositories. We focused on three immunosuppressive signals, TGF-β1, TRAIL and PGE2, modeled by CytoSig. Other signals, such as PD-L1 and IDO, do not have sufficient treatment response data in public repositories thus are not included in the CytoSig model.

Other immunosuppressive signals modeled by CytoSig include IL-4, IL-10 and VEGFA. However, the literature reports a complex relationship between IL-4, IL-10 and CD8<sup>+</sup>T cell function, which discouraged us from including IL-4 and IL-10 in the Tres model.

Concerning CD8<sup>+</sup>T cell function, IL-4 can act as a promoter, an inhibitor or it may have no effect<sup>71</sup>. In particular, previous studies showed that IL-4 could potentiate the cytotoxic activity of CD8<sup>+</sup>T cells during tumor clearance in murine models<sup>23</sup>.

In addition to the immunosuppressive functions of IL-10, some studies reported that IL-10 and PEGylated IL-10 activate the cytotoxicity and proliferation of CD8<sup>+</sup>T cells in mice<sup>72,73</sup> and patients<sup>23</sup>.

The VEGFA activity predicted by CytoSig is not correlated with lower T cell proliferation (median correlation of 0.054; Extended Data Fig. 1a). Thus, our computational model cannot capture the T cell-suppressive function of VEGFA. A potential explanation is that VEGFA primarily suppresses T cell infiltration<sup>74</sup> instead of survival and proliferation modeled by Tres.

**Variable interaction model to identify Tres signatures.** To evaluate whether T cells with high expression of a gene  $G$  are resilient to immunosuppressive signals, we utilized a variable interaction test in multivariate linear regression. We first defined the following variables for individual cells in a single-cell RNA-seq dataset.

Suppression<sub>TGF-β1|TRAIL|PGE2</sub> indicates the immunosuppression level from TGF-β1, TRAIL and PGE2 signaling, predicted using CytoSig<sup>19</sup>.

Proliferation indicates the T cell proliferation score, computed through a linear regression approach. The output variable is the single-cell RNA-seq transcriptome. The explanatory variable is a binary vector with value 1 for all genes in the cell cycle and DNA replication pathways from the KEGG database; and value 0 for all other genes in KEGG. Similarly, we can also compute the T cell cytotoxicity score using a gene set, including GZMA, GZMB, GZMM, GZMK, GZMH and PRF1. The proliferation score is computed as the  $t$  value (Coefficient / StdErr) of the explanatory variable, representing whether a T cell is proliferative or cytotoxic.

$G$  represents the expression level of gene  $G$  across CD8<sup>+</sup>T cells in a tumor.

For each gene  $G$ , we performed the following regression for each cytokine:  $d + a \times \text{suppression} + b \times G + c \times \text{suppression} \times G = \text{proliferation}$

The Tres score is defined as the  $t$  value:  $c / \text{StdErr}(c)$ , estimated through the ordinary least squares.

To further understand the variable interaction test, we can rewrite the model as follows:

$$d + b \times G + (a + c \times G) \times \text{suppression} = \text{proliferation}$$

The association between immunosuppression and proliferation is  $(a + c \times G)$ . The coefficient  $a$  is typically negative because a high immunosuppression activity from TGF-β1, TRAIL and PGE2 signaling results in a low T cell-proliferation level (Fig. 1b and Supplementary Table 2). With a positive gene expression level, a positive coefficient  $c$  will reduce the negative association between immunosuppression and T cell proliferation, whereas a negative coefficient will enhance the negative association.

In single-cell RNA-seq data, some genes have mostly zero counts across cells, known as the dropout phenomenon. Tres will skip all genes with >95% zero counts across T cells in a tumor or if the Cholesky decomposition during regression fails numerically due to a high dropout rate.

**Algorithm.** The complexity of the Tres model is described as follows.

The asymptotic time and memory usage of Tres comprises three parts, enumerated below.

	Time complexity	Memory complexity
CytoSig signaling activity	$(p_1)^2 \times n + p_1 \times n \times m \times n_{\text{rand}}$	$n \times m$
Proliferation signature	$(p_2)^2 \times n \times m$	$n \times m$
Interaction regression	$(p_3)^2 \times m \times n$	$n \times m$

$p_1$ , number of cytokines in the CytoSig expanded model, which is 51.

$p_2$ , number of covariates in proliferation signature regression, which is 2.

$p_3$ , number of covariates in interaction regression, which is 4.

$n$ , number of human genes.

$m$ , number of single cells.

$n_{\text{rand}}$ , number of randomizations, which is 1,000 by default.

Because  $p_1$ ,  $p_2$  and  $p_3$  are all constant, the asymptotic time complexity is

$O(n \times m \times n_{\text{rand}})$  and the asymptotic memory space is  $O(n \times m)$ . As an example of resource usage, the test dataset in the Tres source code package has  $n=23,686$  and  $m=234$ . The running time and memory usages are 167.8 s and 377.2 megabytes, respectively, on a Macbook Pro laptop with 2.6 GHz six-core i7 CPU and 32 GB 2,400 MHz main memory. In another 10X Genomics data example from GSE163108, the dimension is  $n=14,602$  and  $m=25,256$ . The running time and memory usages are 4,194.0 s and 6,692.4 megabytes, respectively on the sample laptop.

**Framework implementation.** The Tres model was implemented using Python v.3.8.8 with dependencies on CytoSig v.0.1 and GCC v.4.8.5. The Tres web server was implemented using Django v.4.0.1, Python v.3.8.8 and MySQL v.8.0.27.

**Statistics and reproducibility.** The pathway enrichment analysis on RNA-seq data was performed using IPA v.70750971. The GSEA on Tres gene scores was performed using GSEA v.4.2.3. All statistical tests comparing group values were performed using Python v.3.8.8 with scipy v.1.7.1. All comparisons between two groups used a Wilcoxon rank-sum test, a nonparametric test without any assumptions on data distribution. Similarly, all comparisons between group values and zero used a nonparametric Wilcoxon signed-rank test.

No data were excluded from any analyses. No statistical method was used to predetermine sample size. For the adoptive T cell transfer experiment (Fig. 5), we selected the mouse sample size as 15 per group, because our recent study demonstrated that 5–10 mice per group was sufficient to achieve statistical significance on treatment response comparisons<sup>75</sup>. For other experiments, we choose a minimal sample size of three for statistical comparisons between groups, which is the lowest sample size to achieve  $P=0.05$  using a two-sided Wilcoxon rank-sum test.

For the adoptive T cell transfer experiment, initially, tumor-bearing mice were randomly distributed into different treatment groups by shuffling their identities. Then, tumor sizes were measured in a double-blinded manner by technicians twice a week. Other experiments were not randomized and investigators were not blinded to allocation and outcome assessment because the robust phenotype of our result is based on strictly objective measurements by equipment instead of any human estimations.

**Human specimens.** Healthy human donor CD8<sup>+</sup>T cells transduced with a recombinant TCR specific for the NY-ESO-1 antigen (NY-ESO-1:157–165 epitope) were provided as a gift by R. Kishton from the Surgery Branch at the NCI, National Institutes of Health (NIH). All human specimens were collected with informed consent and procedures approved by the NCI Institutional Review Board.

**Mice.** All animal experiments were approved by the NCI Animal Ethics Committee of NIH and performed strictly according to the animal protocol CDSL-001, or conducted under protocol 4924-19, approved by the Committee of the Use of Live Animals in Teaching and Research at the University of Hong Kong. C57BL/6 mice were purchased from the Charles River Laboratories (NCI strains). Female mice at 6–8 weeks of age were used for tumor incubation and T cell transfer experiments. The maximal tumor size permitted by the ethics committee is 2 cm in diameter and no tumor burden exceeded that limit in our experiment. Pmel-1 TCR transgenic mice were provided as a gift by C.-P. Dai from the Merlino Laboratory at NCI, NIH. Mice were housed on 12 h light-dark cycles with the ambient temperature at 20–25 °C and 40–60% humidity.

**Cell lines and cultures.** The human melanoma cell line A375 was recently purchased from the American Type Culture Collection (CRL-1619). Mel624 and B16-mhgp100 were provided as a gift by R. J. Kishton from the Surgery Branch at NCI, NIH. Mel624 cells were established in the Surgery Branch, NCI from resected tumors. B16 (H-2b), the original source of B16-mhgp100, is a gp100<sup>+</sup> spontaneous murine melanoma obtained from the NCI tumor repository.

A375, Mel624 and B16-mhgp100 cells were routinely cultured in RPMI 1640 medium (Gibco) supplemented with 10% FBS (Gibco BRL) and 100 IU ml<sup>-1</sup> penicillin/streptomycin (P/S). The 293FT cells (Thermo Fisher, R70007)

were cultured in complete medium, which is high-glucose DMEM (Gibco) supplemented with 10% FBS (Gibco BRL), 100 IU ml<sup>-1</sup> P/S, 1 mM sodium pyruvate (Gibco), 0.1 mM MEM NEAA (Gibco) and 0.5 mg ml<sup>-1</sup> geneticin (Gibco). All cells were incubated in a humidified incubator at 37 °C with a 5% CO<sub>2</sub> supply.

**tdTomato labeling on cancer cells.** A375, Mel624 and B16-mhgp100 cells were labeled with tdTomato via lentiviral transduction for cell growth assays through the Incucyte experiments.

The 293FT cells were seeded at a density of 1 × 10<sup>6</sup> cells per well in a six-well plate in a complete culture medium. The next day (day 2), cells were transfected with pLenti-V6.3 Ultra-Chili (Addgene, 106173) plasmid, together with the packaging plasmids psPAX2 (Addgene, 12260) and pMD2.G (Addgene, 12259) using the Lipofectamine 2000 transfection reagent (Invitrogen, 11668030) according to the manufacturer's protocol. On day 3, we replaced the supernatant with a fresh transfection medium supplemented with a viral boost reagent (500×, Alstern, VB100) as per the manufacturer's instructions. The virus was collected by spinning down the viral supernatant at 1,000g, 4 °C for 15 min to remove the cell debris at day 4.

A375, Mel624 and B16-mhgp100 cells were mixed with lentivirus at the 1:1 dilution with culture medium, 10 µg ml<sup>-1</sup> polybrene (Sigma, TR-1003) was added to the mixture for 24 h before refreshing the medium. Three days after infection, blasticidin (Gibco, A1113903) was added for the selection and maintenance of cells with positive tdTomato expression.

**Preparation of human donor CD8<sup>+</sup> T cells.** Human NY-ESO-1 CD8<sup>+</sup> T cells were stimulated with plate-bound anti-human CD3 (TONBO, 40-0038-U100, clone UCHT1) at 10 µg ml<sup>-1</sup> and anti-human CD28 (TONBO, 40-0289-U100, clone CD28.2) at 2 µg ml<sup>-1</sup> for 48 h before expanded with recombinant human IL-2 (BioLegend, 589106) at 100 IU ml<sup>-1</sup>. Cells were cultured in completed X-Vivo medium, which is X-Vivo 15 Serum-free Hematopoietic Cell Medium (Lonza, BE02-060Q) supplemented with 5% inactivated FBS (Gibco, 10082147), 50 µM 2-mercaptoethanol (Gibco, 21985023) and 10 mM N-acetyl L-cysteine (Sigma, A7250-5G) at 1 × 10<sup>6</sup> cells per ml.

**Preparation of mouse CD8<sup>+</sup> T cells.** CD8<sup>+</sup> T cells were isolated from the single-cell suspension of splenocytes of Pmel-1 TCR transgenic or regular mice using the EasySep mouse CD8<sup>+</sup> T cell isolation kit (STEMCELL, cat. no. 18953) by negative magnetic selection. If cells were not used directly, the freshly isolated splenocytes were frozen in a cryopreservation medium (Gibco, cat. no. 2176664). CD8<sup>+</sup> T cells isolated from newly thawed splenocytes using the same method were rested in the medium overnight before stimulation. Isolated CD8<sup>+</sup> T cells were stimulated with plate-bound anti-mouse CD3 (TONBO, 40-0032-U100, clone 17A2) at 10 µg ml<sup>-1</sup> and anti-mouse CD28 (TONBO, 40-0281-U100, clone 37.51) at 5 µg ml<sup>-1</sup> for 48 h before being expanded with recombinant mouse IL-2 (BioLegend, 575406) at 100 IU ml<sup>-1</sup>.

Cells were cultured in complete RPMI 1640 medium, which is RPMI 1640 medium (Gibco, 11875119) supplemented with 10% inactivated FBS (Gibco, 10082147), 20 mM HEPES (Gibco, 15630080), 1 mM sodium pyruvate (Gibco, 11360070), 50 µM 2-mercaptoethanol (Gibco, 21985023), 2 mM L-glutamine (Gibco, 25030024) and 1% P/S (Gibco, 15140122) at 1 × 10<sup>6</sup> cells per ml.

**Cas9 ribonucleotide protein nucleofection.** Lyophilized tracrRNA (IDT, 1072533) and crRNA (predesigned and synthesized from IDT, the oligonucleotides targeting different genes are listed at Supplementary Table 9a) were resuspended in duplex buffer (IDT, 11-01-03-01) to 100-µM stock concentrations. CrRNA and tracrRNA were combined at a 1:1 volume ratio and incubated at 95 °C for 5 min in sterile PCR tubes in the thermocycler. The gRNA complexes were then cooled down at room temperature for 20–30 min. Cas9 protein (Berkeley MacroLab, 40 µM) was added to the crRNA-tracrRNA complexes at a 1:2 volume ratio and incubated at room temperature for 15 min. Assembled Cas9 ribonucleotide proteins (Cas9-RNP) were aliquoted to the PCR tube at 5 µl per tube.

Pre-activated mice or human CD8<sup>+</sup> T cells were spun down and resuspended in the Lonza P3 buffer at 1 × 10<sup>6</sup> cells per 20 µl and 60 µl cell resuspension was added to the PCR tube. The cell–Cas9-RNP mixtures were transferred to a 100-µl nucleofection cuvette (Lonza, V4XP-3024) and electroporated using the pulse program CM137 for mice activated T cells and EH100 for human activated T cells. After nucleofection, 100 µl pre-warmed culture medium was immediately added to the cuvettes and cells were transferred to a six-well plate at a density of 1 × 10<sup>6</sup> cells per ml.

**Fibp overexpression in mice primary CD8<sup>+</sup> T cells.** The ORF of mice *Fibp* gene with three Flag tags at the N terminus and fused eGFP at the C terminus was cloned into the pCDH-EF1-MCS-IRES-puro vector (provided by X.-Y. Guan's laboratory at the University of Hong Kong).

The 293FT cells were seeded at the density of 1 million cells per well in a six-well plate in complete culture medium. The next day (day 2), cells were transfected with the *Fibp* overexpression plasmid, together with the packaging plasmids psPAX2 (Addgene, 12260) and pMD2.G (Addgene, 12259) using the Lipofectamine 2000 transfection reagent (Invitrogen, 11668030) according to the manufacturer's protocol. On day 3, we replaced the supernatant with a fresh transfection medium supplemented with the viral boost reagent (500×, Alstern,

VB100) as per the manufacturer's instructions. The virus was collected by spinning down the viral supernatant at 1,000g, 4 °C for 15 min to remove the cell debris at day 4.

To concentrate virus particles, we mixed the virus with the precipitation solution (Alstern, VC100) per the manufacturer's protocols, refrigerated at 4 °C for 4 h and spun down at 1,500g for 30 min at 4 °C. The pellet was resuspended in cold PBS to make the 100× concentrated lentivirus.

Mice primary CD8<sup>+</sup> T cells (2 million ml<sup>-1</sup>) were cultured with the concentrated lentivirus (50 µl ml<sup>-1</sup>) supplemented with 8 µg ml<sup>-1</sup> polybrene and centrifuged at 500g at 32 °C for 90 min. The medium was refreshed 12 h later and cells were cultured in complete culture medium.

**RT-qPCR analysis.** Total RNA was extracted from T cells using TRIzol reagent (Thermo Fisher, 15596026) and cDNA was synthesized through reverse transcription using the PrimeScript RT Reagent kit with gDNA eraser (Takara, RR047A). RT-qPCR was performed using the TB green Premix Ex Taq kit (Takara, RR420A) and corresponding primers. Ct values were detected by StepOne Plus Real-time PCR system. Raw data were processed using SDS 19.1 software and the relative mRNA expression level was normalized to the internal reference gene ACTB. The primer sequences are listed in Supplementary Table 9b.

**Western blot.** A total of 5 × 10<sup>6</sup> T cells from each sample were collected. Cell pellets were washed with cold PBS three times and lysed with RIPA buffer (Thermo Fisher, 89900) supplemented with protease and phosphatase inhibitor cocktail (Thermo Fisher, 78441). After protein quantification using the BSA method, samples were separated on the NuPAGE 4–12% Bis-Tris Gel (Invitrogen), transferred to nitrocellulose membrane (Life Technologies), blocked with 5% non-fat milk in TBST and incubated with primary antibodies at 4 °C overnight. Signals were detected using HRP-conjugated secondary antibodies and ECL western blotting detection reagent (GE healthcare). Primary and secondary antibodies are listed in Supplementary Table 9c. All raw western blot images are provided in Supplementary Figs. 1, 4 and 5 and labeled in the source data file associated with each figure.

**Flow cytometry analysis.** For the evaluation of surface and intracellular markers on CD8<sup>+</sup> T cells, antibodies and dyes are listed in Supplementary Table 9c,d. Flow cytometry was performed on the BD LSR Fortessa SORP I instrument, FACS CantoII analyzer, BD FACSymphony and ACEA Novocyte Quanteon. Raw data were analyzed using FlowJo software (v.10.6.1).

For the *in vivo* multidimensional analysis of tumor-infiltrating CD8<sup>+</sup> T cells, tumors were collected on day 9–12 after CD8<sup>+</sup> T cell transfer, manually minced and incubated in RPMI 1640 medium containing DNase I (200 µg ml<sup>-1</sup>, Sigma, DN-25) and Liberase (100 µg ml<sup>-1</sup>, Sigma, 5401020001) for 30 min at 37 °C. The dissociated cells were then passed through a 70-µM cell strainer (BD Falcon, 352350). CD8<sup>+</sup> T cells were enriched from the filtered cells using CD8<sup>+</sup> TIL microbeads (Miltenyi, 130-116-478) according to the manufacturer's instructions. Cells were then stained with cell-surface antibodies. DAPI was used to identify dead cells. For Filipin III staining, dead cells were marked using Zombie NIR fixable viability kit (BioLegend, 423105) before fixation and staining.

Tumors with a size of less than 10 mm<sup>2</sup> were excluded from analysis because the amount of tumor-infiltrating T cells was not sufficient for flow cytometry. The maximum tumor diameter permitted by animal committees is 2 cm and this maximum tumor size was not exceeded.

We used the forward-scatter area or height (FSC-A or FSC-H) and side-scatter area or height (SSC-A or SSC-H) for dead cell and debris removal. The forward-scatter height (FSC-H), width (FSC-W), side-scatter height (SSC-H) and width (SSC-W) are used to gate the single cells. To analyze CD8<sup>+</sup> TILs, we also included DAPI/Zombie NIR and CD8 to identify live CD8<sup>+</sup> T cells. We include unstained cells to define the threshold separating positive populations from negative control cells. Gating strategies are demonstrated in Extended Data Figs. 6e, 7f and 9a,c.

**CFSE staining.** We spun down one vial of lyophilized CFSE dye (BioLegend, 423801) and reconstituted it in 36 µl of DMSO to make the 5 mM stock solution according to the manufacturer's instructions. We prepared the 5 µl working solution of CFSE dye by 1:1,000 dilution of the 5 mM stock solution in PBS immediately before use. After spinning down the cells at 90g for 10 min and resuspending the cells at 1 × 10<sup>7</sup> cells per ml in the CFSE working solution, we incubated cells at room temperature for 20 min in the dark and then quenched the staining with five times the volume of complete culture medium. Finally, we spun down and resuspended cells in a regular culture medium before restimulation or simvastatin treatment.

**Cancer cell and T cell *in vitro* co-culture assay.** We used two settings: (1) A375, Mel624 tumor cell lines and human NY-ESO-1 T cells; and (2) B16-mhgp100 cells and mice Pmel-1 T cells. Cancer cells were seeded at different densities in 100 µl of complete culture medium in the 96-well plate (for A375 and Mel624 cells, 5,000 cells per well; for B16-mhgp100 cells, 2,500 cells per well). The next day, CD8<sup>+</sup> T cells were resuspended in complete medium and added at 50 µl per well on top of tumor cells at the effector-to-target ratio of 2:1 or 4:1.

In the experiments involving cholesterol (Sigma, C4951) treatment, T cells were pre-treated with cholesterol at the indicated concentration for 5 d and then washed before adding to the co-culture system. The plates were then subjected to the Incucyte real-time cell imaging system and the intensity of tdTomato labeling on tumor cells was counted over time.

**ELISA.** To detect the levels of cytokines released by T cells after co-culture with tumor cells, we seeded the tumor cells A375 and B16-mhgp100 in 100 µl complete culture medium in a 96-well plate (for A375, we seeded  $1 \times 10^5$  cells per well and for B16-mhgp100, we seeded  $5 \times 10^4$  cells per well). The next day, the matched human NY-ESO-1 or mice Pmel-1 edited CD8<sup>+</sup>T cells were added on top of tumor cells at an effector-to-target ratio of 2. At 6 h later, the supernatant was collected and the TNF secretion level was detected using the TNF- $\alpha$  DuoSet ELISA kit (R&D DY410 and DY210). According to the manufacturer's instructions, the amount of IFN- $\gamma$  was determined with supernatant collected 24 h later using the IFN- $\gamma$  DuoSet ELISA kit (R&D, DY485 and DY285B).

**Adoptive T cell transfer.** For adoptive T cell transfer therapy, we used B16-mhgp100 cells responsive to Pmel-1 CD8<sup>+</sup>T cells in the C57BL/6 mouse model. A total of  $5 \times 10^5$  B16-mhgp100 cells were injected subcutaneously into the right flank of C57BL/6 mice. At 9–10 d after tumor implantation, mice were sublethally irradiated with the dose of 600 cGy and randomly distributed into different treatment groups. The next day,  $1 \times 10^6$  edited CD8<sup>+</sup>T cells (7 d after Cas9-RNP nucleofection) were transferred intravenously into the mice and recombinant human IL-2 was given ( $1 \times 10^5$  IU  $0.5 \text{ ml}^{-1}$ ) by intraperitoneal injection twice daily for 3 d consecutively. PBS and primary T cells without editing were used as controls. Tumor size was measured in a double-blinded manner twice a week after T cell transfer and the tumor area was calculated as length  $\times$  width. Mice were killed when either diameter reached 2 cm and this maximum tumor size was not exceeded.

**Whole-transcriptome sequencing.** A total of  $2 \times 10^6$  T cells from each sample were collected. The cell lysate was incubated with 500 µl TRIzol reagent at room temperature for 5 min. We added 100 µl chloroform to each sample and shook the tube vigorously by hand for 15 s. We incubated at room temperature for 5 min and then centrifuged at 12,000g for 15 min at 4 °C. We transferred the upper phase to a new tube and added an equal volume of 70% ethanol. The vortexed mixture was subjected to binding, washing and elution steps using the PureLink RNA Mini kit (Thermo Fisher, 12183020). RNA was then treated with DNase I (Thermo Fisher, 89836) for genomic DNA removal according to the manufacturer's instructions. The RNA integrity number values of all samples were above 8.0.

**Cellular cholesterol content measurement.** Cellular-free cholesterol content was measured using the cholesterol cell-based detection assay kit (Cayman, 10009779). Cells were fixed, washed and stained with Filipin III before being analyzed using the BD FACSymphony flow analyzer and BD LSR Fortessa SORP I instrument. For the oxidation-based quantification of cholesterol, total cholesterol was extracted using the cholesterol extraction kit (Sigma, MAK175) and then analyzed using the Amplex Red Cholesterol Assay kit (Invitrogen, A12216) per the manufacturer's instructions.

**LDL uptake assay.** For LDL uptake experiments in primary mouse CD8<sup>+</sup>T cells with *Filp* knockout, cells were starved in low-glucose RPMI 1640 (Gibco, 21870076), complemented with low glutamine (1 mM), 0.3% BSA instead of standard FBS for 16 h. Then, diluted LDL-Dylight 488 (Cayman, 601470) was added to each well at the dilution of 1:200. Cells were incubated at 37 °C for 4 h in the dark. Staining was measured by flow cytometry using the FACS CantoII analyzer.

**Simvastatin treatment.** Simvastatin (Sigma, PHR1438) was provided as a solid powder and dissolved in DMSO at a stock concentration of 20 mM at –80 °C. CD8<sup>+</sup>T cells isolated from C57BL/6 mice splenocytes were stained with CFSE dye as described in the Methods section 'CFSE staining'. Then, T cells were stimulated with anti-mouse CD3/28 and treated with simvastatin at several concentrations (0, 1, 5, 10 and 20 µM) simultaneously. The same CFSE staining and treatment of simvastatin were applied to CD8<sup>+</sup>T cells after stimulation and during expansion with IL-2 for 3 d. At the end of treatment, cells were collected and washed before Filipin III and CFSE detection by flow cytometry.

**Reporting Summary.** Further information on research design is available in the Nature Research Reporting Summary linked to this article.

## Data availability

The RNA-seq data generated by this study have been deposited to the NCBI Gene Expression Omnibus with accession ID GSE186428. All flow analysis raw data are available in FCS format at the Flowrepository<sup>76</sup> with accession IDs as listed in Supplementary Table 10 and source data tables for each figure. All gene scores computed by the Tres model are available at <https://resilience.ccr.cancer.gov>.

For public datasets, single-cell RNA-seq data collected from public studies for training Tres signatures are listed in Supplementary Table 1. T cell transcriptomic data for validating the Tres model are available for download as processed data at [https://github.com/data2intelligence/Tres\\_main](https://github.com/data2intelligence/Tres_main). Bulk-tumor transcriptomic datasets of ICI pretreatment tumors are listed in Supplementary Table 4. Public ChIP-seq profiles of SREBF2 were originally available from GSE31477 and binding peak calls reprocessed by the Cistrome pipeline are available at <http://cistrome.org>. The CCLE cancer cell line expression profiles are available from <https://depmap.org>. Genome-wide CRISPR screen data on human donor T cells are downloaded from supplementary materials of the original studies<sup>12,13</sup> and GSE174255. The MILE leukemia dataset is available from GSE13159.

For public databases, TIDE is available at <http://tide.dfci.harvard.edu>. Cistrome is available at <http://cistrome.org>. MSigDB, which provides KEGG gene sets (v.7.4) of cell cycle and DNA replication, is available at <https://www.gsea-msigdb.org>.

Source data for all main and extended data figures are provided. Raw western blots are shown in Supplementary Figs. 1, 4 and 5. Raw Incucyte images are shown in Supplementary Fig. 2. Source data are provided with this paper.

## Code availability

The interactive Tres server is available at <https://resilience.ccr.cancer.gov>. The source code and test data for the Tres model and T cell efficacy prediction are available at <https://github.com/data2intelligence/Tres>. The programs for reproducing major results, including computing Tres signatures and predicting immunotherapy response, are available at [https://github.com/data2intelligence/Tres\\_main](https://github.com/data2intelligence/Tres_main). Source data are provided with this paper.

## References

70. Xi, H. et al. A human skeletal muscle atlas identifies the trajectories of stem and progenitor cells across development and from human pluripotent stem cells. *Cell Stem Cell*. <https://doi.org/10.1016/j.stem.2020.04.017> (2020).
71. Silva-Filho, J. L., Caruso-Neves, C. & Pinheiro, A. A. S. IL-4: an important cytokine in determining the fate of T cells. *Biophys. Rev.* <https://doi.org/10.1007/s12551-013-0133-z> (2014).
72. Emmerich, J. et al. IL-10 directly activates and expands tumor-resident CD8<sup>+</sup>T cells without de novo infiltration from secondary lymphoid organs. *Cancer Res.* **72**, 3570–3581 (2012).
73. Hanna, B. S. et al. Interleukin-10 receptor signaling promotes the maintenance of a PD-1/int TCF-1<sup>+</sup>CD8<sup>+</sup>T cell population that sustains anti-tumor immunity. *Immunity* <https://doi.org/10.1016/j.jimmuni.2021.11.004> (2021).
74. Schaaf, M. B., Garg, A. D. & Agostinis, P. Defining the role of the tumor vasculature in antitumor immunity and immunotherapy. *Cell Death Dis.* **9**, 115 (2018).
75. Pan, D. et al. A major chromatin regulator determines resistance of tumor cells to T cell-mediated killing. *Science*. <https://doi.org/10.1126/science.aoa1710> (2018).
76. Spidlen, J., Breuer, K. & Brinkman, R. Preparing a minimum information about a flow cytometry experiment (MIFlowCyt) compliant manuscript using the International Society for Advancement of Cytometry (ISAC) FCS file repository (FlowRepository.org). *Curr. Protoc. Cytom.* <https://doi.org/10.1002/0471142956.cy1018s61> (2012).
77. Ghandi, M. et al. Next-generation characterization of the Cancer Cell Line Encyclopedia. *Nature* **569**, 503–508 (2019).
78. Duffy, D. J. et al. Integrative omics reveals MYCN as a global suppressor of cellular signalling and enables network-based therapeutic target discovery in neuroblastoma. *Oncotarget* **6**, 43182–43201 (2015).
79. Zheng, R. et al. Cistrome Data Browser: expanded datasets and new tools for gene regulatory analysis. *Nucleic Acids Res.* **47**, D729–D735 (2019).

## Acknowledgements

We thank S. Rosenberg, F. Lowry, K. Sri and M. Carrington for their helpful discussions. This work utilized the computational resources of the NIH HPC Biowulf cluster. This work is supported by the intramural budget allocation from the NCI, NIH, awarded to P.J. Y.Z. is partially supported by a Bau Tsu Zung Bau Kwan Yeu Hing Research and Clinical Fellowship from the University of Hong Kong. T.V. is supported by the NCI iCURE and T2I Postdoc fellowship.

## Author contributions

P.J. and Y.Z. designed the study and wrote the manuscript. P.J. performed all computational analysis and created the Tres package and web server. Y.Z. and T.V. performed wet-laboratory experiments. R.K. provided human donor T cells. C.S. and C.D. provided Pmel-1 TCR transgenic mice. R.P. deployed the Tres server under the government domain. K.A. and X.G. provided the laboratory space. L.G., J.H., F.L., D.P., T.N., Z.C., C.W. and G.M. participated in discussions.

**Competing interests**

NCI, NIH has submitted a provisional patent application no. 63/246,743 for using *FIBP* KO to enhance cellular immunotherapy efficacies, with P.J. and Y.Z. as inventors. All other authors declare no competing interests.

**Additional information**

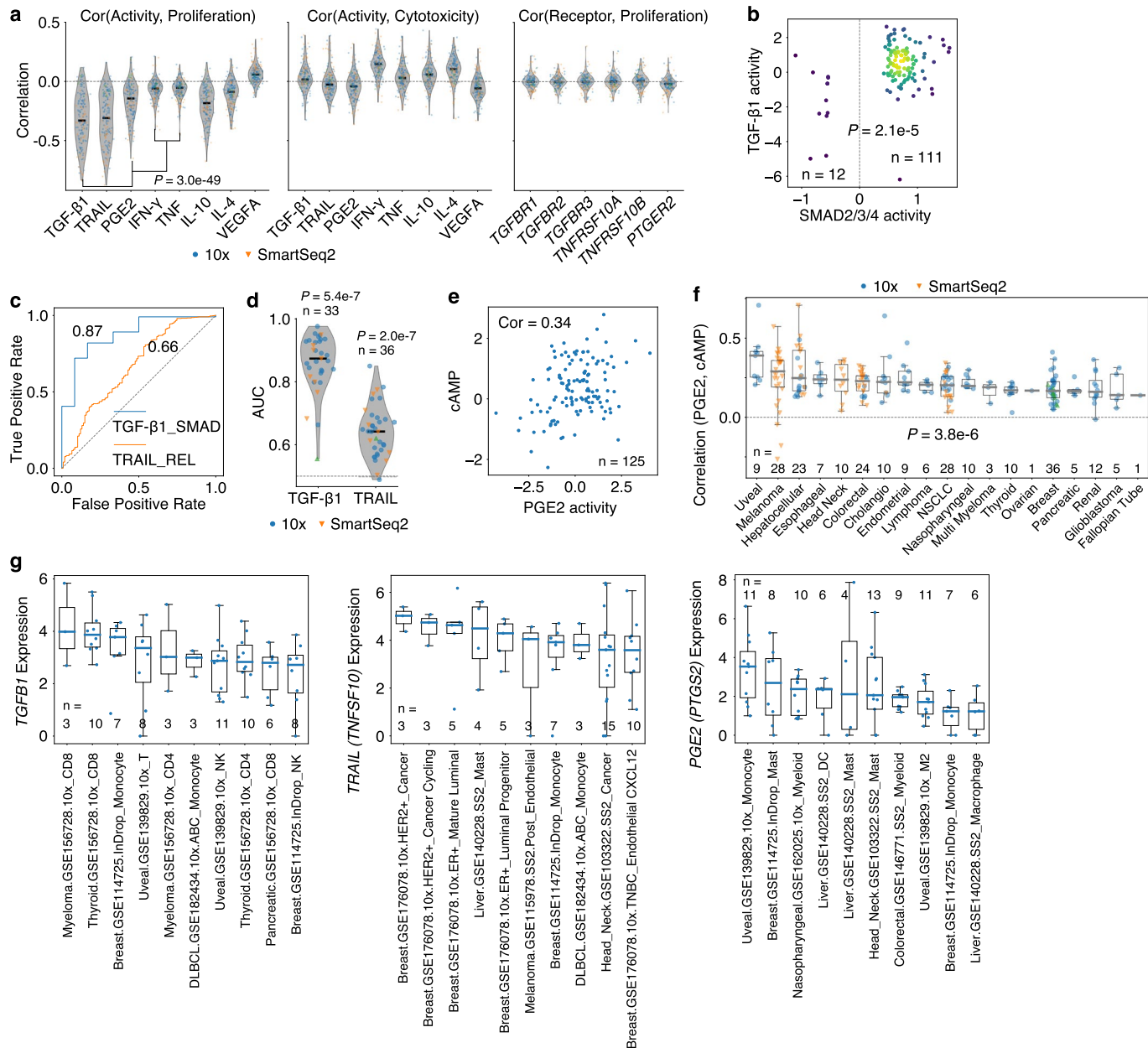
**Extended data** is available for this paper at <https://doi.org/10.1038/s41591-022-01799-y>.

**Supplementary information** The online version contains supplementary material available at <https://doi.org/10.1038/s41591-022-01799-y>.

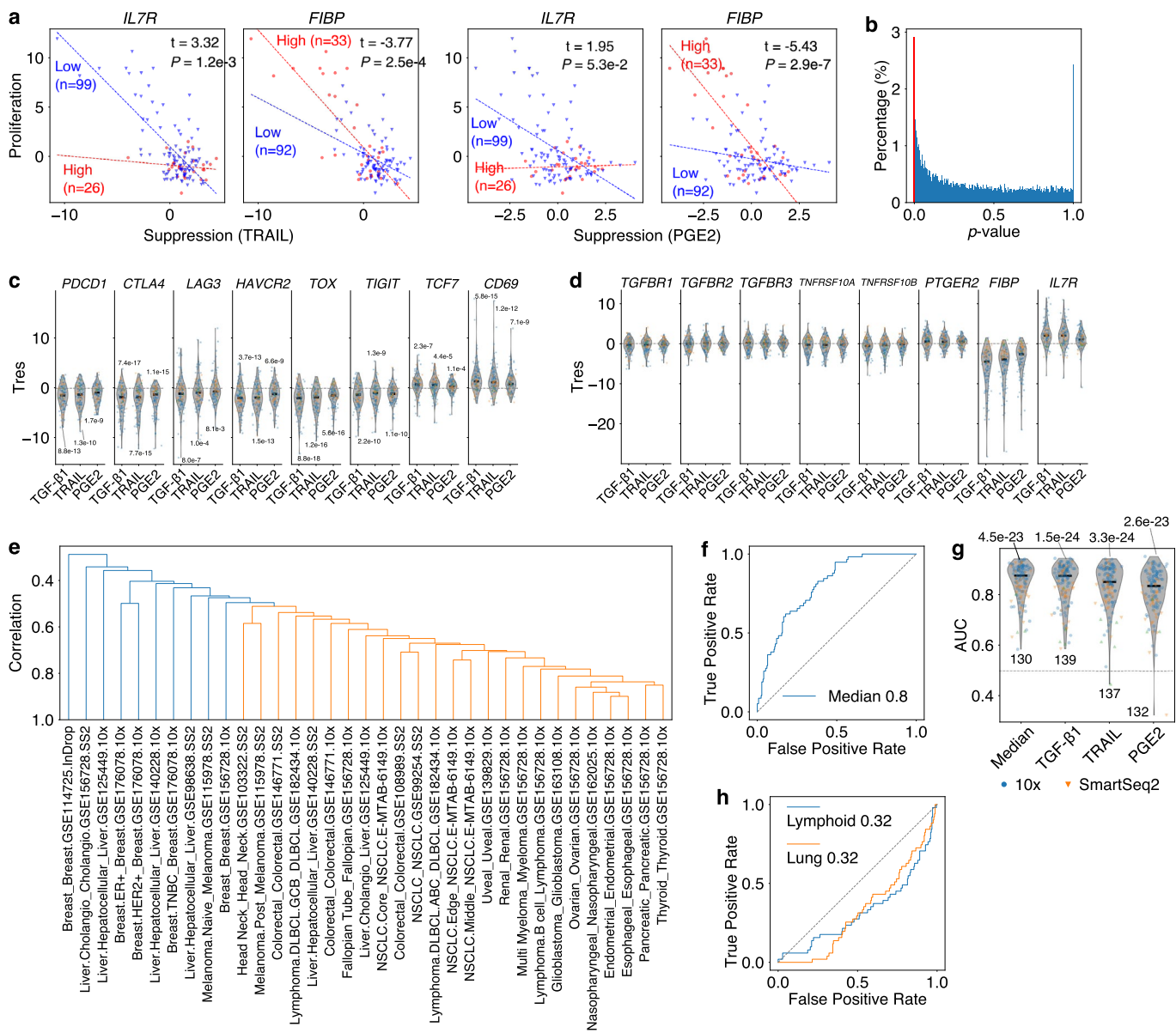
**Correspondence and requests for materials** should be addressed to Peng Jiang.

**Peer review information** *Nature Medicine* thanks Alexander Huang and the other, anonymous, reviewer(s) for their contribution to the peer review of this work. Saheli Sadanand was the primary editor on this article and managed its editorial process and peer review in collaboration with the rest of the editorial team.

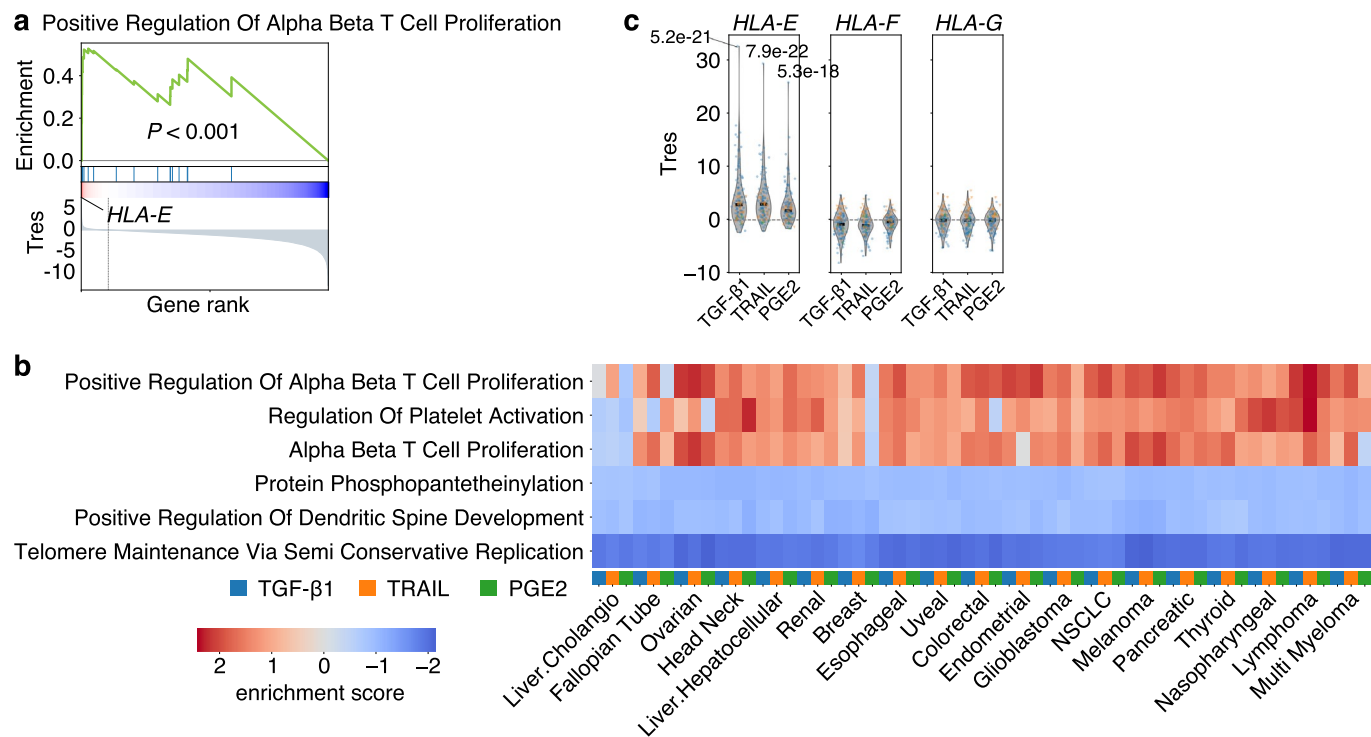
**Reprints and permissions information** is available at [www.nature.com/reprints](http://www.nature.com/reprints).



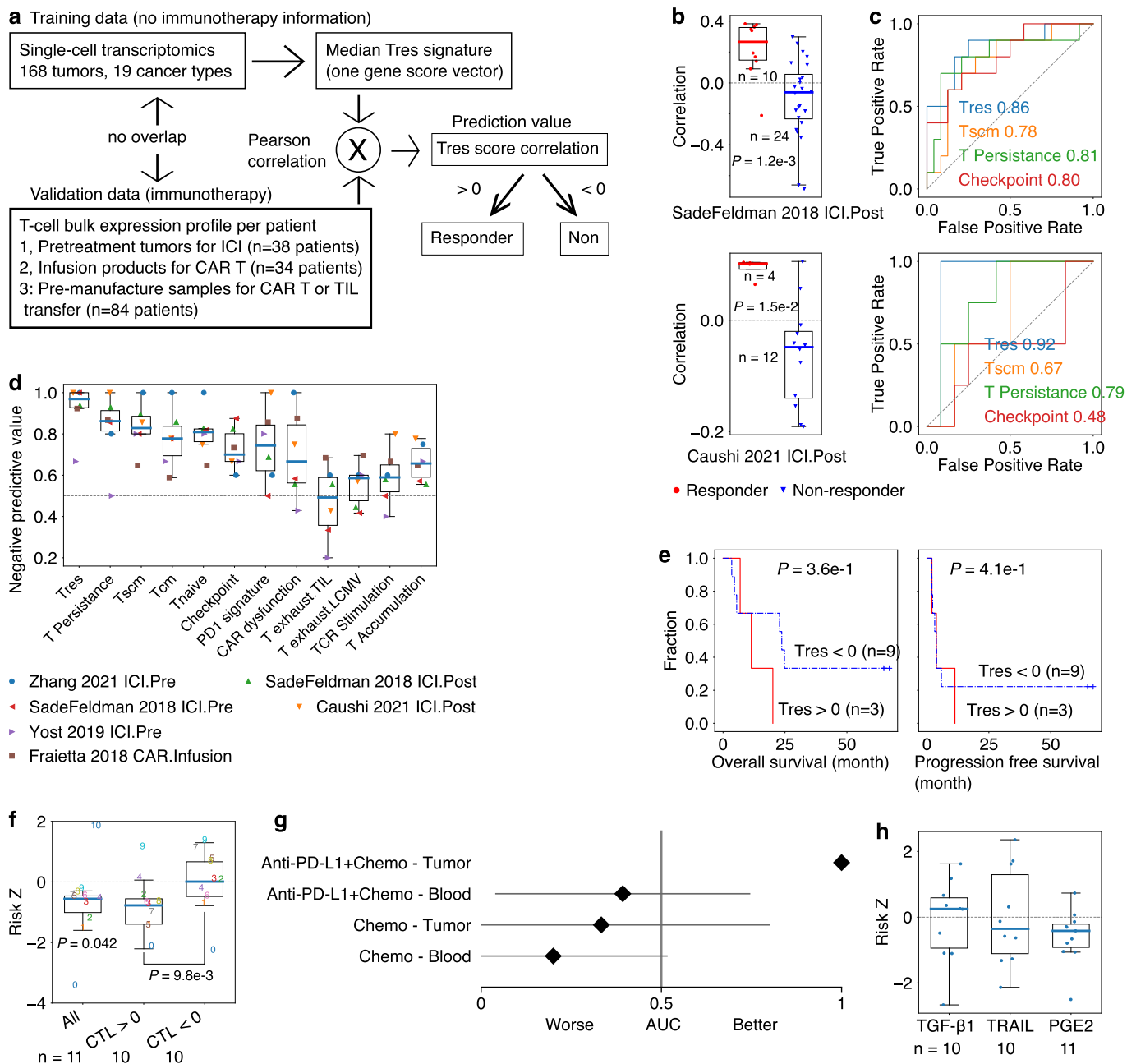
**Extended Data Fig. 1 | Quantifying immunosuppression of T cells in single-cell data.** **a**, Correlations between immunosuppressive signaling and T cell proliferation or cytotoxicity, shown with the violin plot smoothed by a kernel density estimator ( $n=168$  per group). Each dot represents a tumor. The  $p$ -value was from the two-sided Wilcoxon rank-sum test. **b**, Association between TGF- $\beta$ 1 signaling and SMAD transcription factor (TF) activities, an example from a melanoma tumor<sup>18</sup>. Each dot presents a CD8 + T cell. The Y-axis presents the TGF- $\beta$ 1 activities. The X-axis presents the SMAD TF activities. The  $p$ -value was from the two-sided Wilcoxon rank-sum test, comparing TGF- $\beta$ 1 activities between T cells with positive and negative SMAD activities. **c**, Receiver operating characteristic (ROC) curve for the quality of signaling activities. At different thresholds, the ROC curve presents false-positive rates against true-positive rates of predicting SMAD or REL activities through TGF- $\beta$ 1 or TRAIL signaling activities, respectively. The diagonal line represents random expectation. **d**, Quality of signaling activities across single-cell cohorts. Each dot presents a single-cell cohort. The area under the ROC curve (AUC) measures the quality of TGF- $\beta$ 1 or TRAIL signaling, shown with violin plots smoothed by a density kernel estimator.  $P$ -values were from the two-sided Wilcoxon signed-rank test, comparing group values with 0.5 (random expectation). **e**, Correlation between PGE2 signaling and cAMP pathway activities, an example of a melanoma tumor<sup>18</sup>. Each dot represents a CD8 + T cell. The X-axis shows the PGE2 signaling activity. The Y-axis shows the cAMP geneset value. **f**, Correlations between PGE2 signaling and cAMP activities. Each dot represents a tumor. The correlations were shown through box plots. The thick line represents the median value. The bottom and top of the boxes are the 25th and 75th percentiles (interquartile range). Whiskers encompass 1.5 times the interquartile range. The  $p$ -value was from the two-sided Wilcoxon signed-rank test, comparing group medians and zero. **g**, Gene expression of immunosuppressive signals. Each dot represents a patient. Y-axis presents the average gene expression across all cells for each lineage (X-axis). All lineages were ranked by the median expression and only the top ten profiles were shown in box plots as panel f.



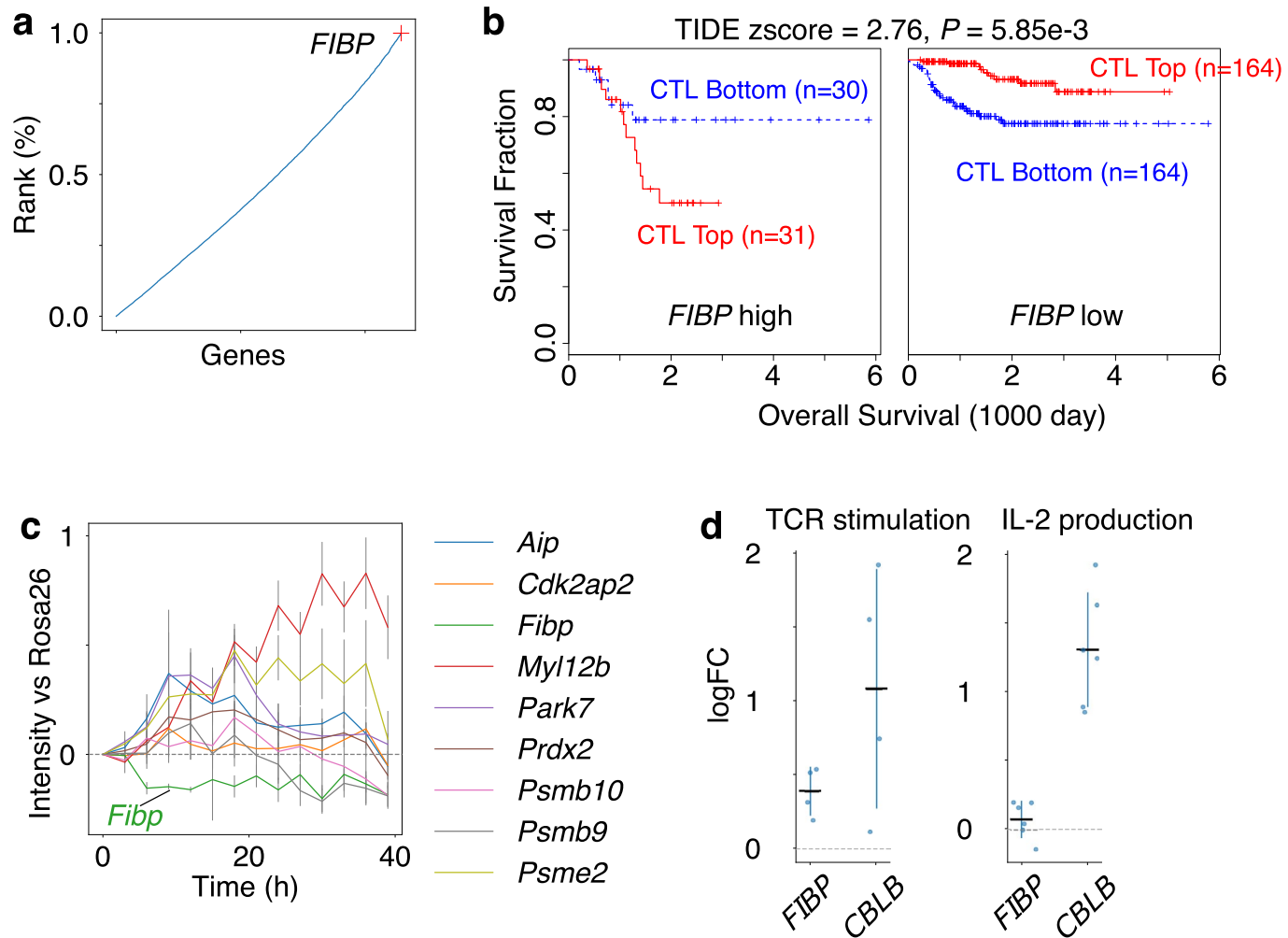
**Extended Data Fig. 2 | Modeling transcriptomic signatures of tumor-resilient T cells.** **a**, Variable interaction test. The correlation between immunosuppression (through TRAIL or PGE2 signaling) and CD8+T cell proliferation is plotted as Fig. 1c. Individual cells were split into high or low groups according to the expression of *IL7R* or *FIBP* (Cutoff = 2).  $P$ -values and  $t$ -values (Tres gene scores) were from the two-sided interaction test using continuous values without any cutoffs. **b**, Distribution of interaction test  $p$ -values, an example from a melanoma tumor #98<sup>18</sup>. Two-sided student t-test  $p$ -values were computed for every gene and shown by a histogram. **c**, Tres gene scores of T cell function markers. Each dot represents a tumor. Tres scores computed for each signal are shown through violin plots smoothed by a kernel density estimator ( $n = 139, 137, 132$  for TGF- $\beta$ 1, TRAIL, PGE2 groups).  $P$ -values were from the two-sided Wilcoxon signed-rank test comparing group values and zero. **d**, Tres gene scores of immunosuppressive signal receptors, shown as panel c. Scores for *FIBP* and *IL7R* are attached as references. **e**, Similarity of Tres scores from different single-cell cohorts. The hierarchical clustering is based on Pearson correlations among median Tres scores among all patients and immunosuppressive signals in each cohort. **f**, Receiver operating characteristic (ROC) curve for the quality of Tres score. The ROC curve presents false-positive rates against true-positive rates of predicting T-cell persistence markers through Tres gene scores at different thresholds, using the example data in Fig. 1e. The diagonal line represents random expectation. The area under the ROC curve (AUC) is a quantitative measure of Tres score quality. **g**, Quality of Tres scores. Each dot represents a tumor with sample counts labeled beneath each group. The AUC in each cohort was shown through violin plots, smoothed by a kernel density estimator.  $P$ -values (labeled above each group) were computed through the two-sided Wilcoxon signed-rank test, comparing the group values and the random expectation 0.5. **h**, ROC curves for Tres scores computed using *in vitro* cell line data from the CCLE project<sup>7</sup>. Results from the two most frequent lineages (with more than 100 cell lines) are shown as panel f.



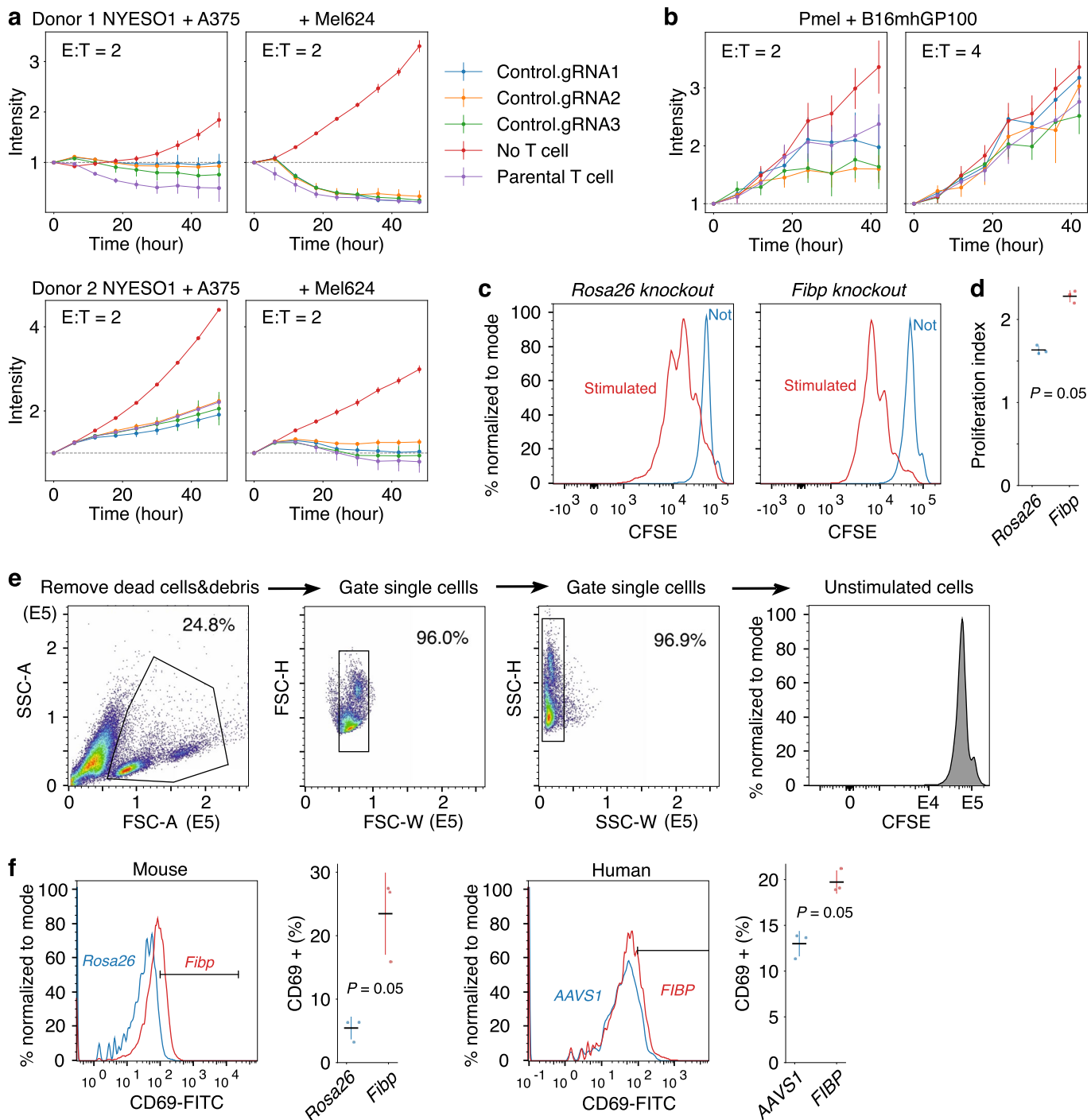
**Extended Data Fig. 3 | Geneset enrichment analysis for Tres gene scores.** **a**, Gene set enrichment analysis (GSEA)<sup>25</sup>, an example on  $\alpha\beta$  T cell proliferation. X-axis presents the gene ranked by median Tres scores (bottom Y-axis) across all tumors and immunosuppressive signals. Y-axis on the top presents enrichment scores at each gene rank. The  $P$ -value is computed through the two-sided permutation test ( $n=1000$  randomizations). *HLA-E* is the first gene annotated in the pathway. **b**, Top-three enriched biological processes. For each cancer type, enrichment of gene ontology pathways was analyzed for median Tres scores among all patients. Top-three enriched and depleted pathways for Tres scores related to TGF- $\beta$ 1, TRAIL and PGE2 signaling were shown together. **c**, Tres scores of non-classical MHC class I molecules. Each dot represents a value from a tumor. Tres scores computed for each signal are shown through violin plots smoothed by a kernel density estimator ( $n=139, 137, 132$  for TGF- $\beta$ 1, TRAIL, PGE2 groups).  $P$ -values were from the two-sided Wilcoxon signed-rank test comparing group values and zero.



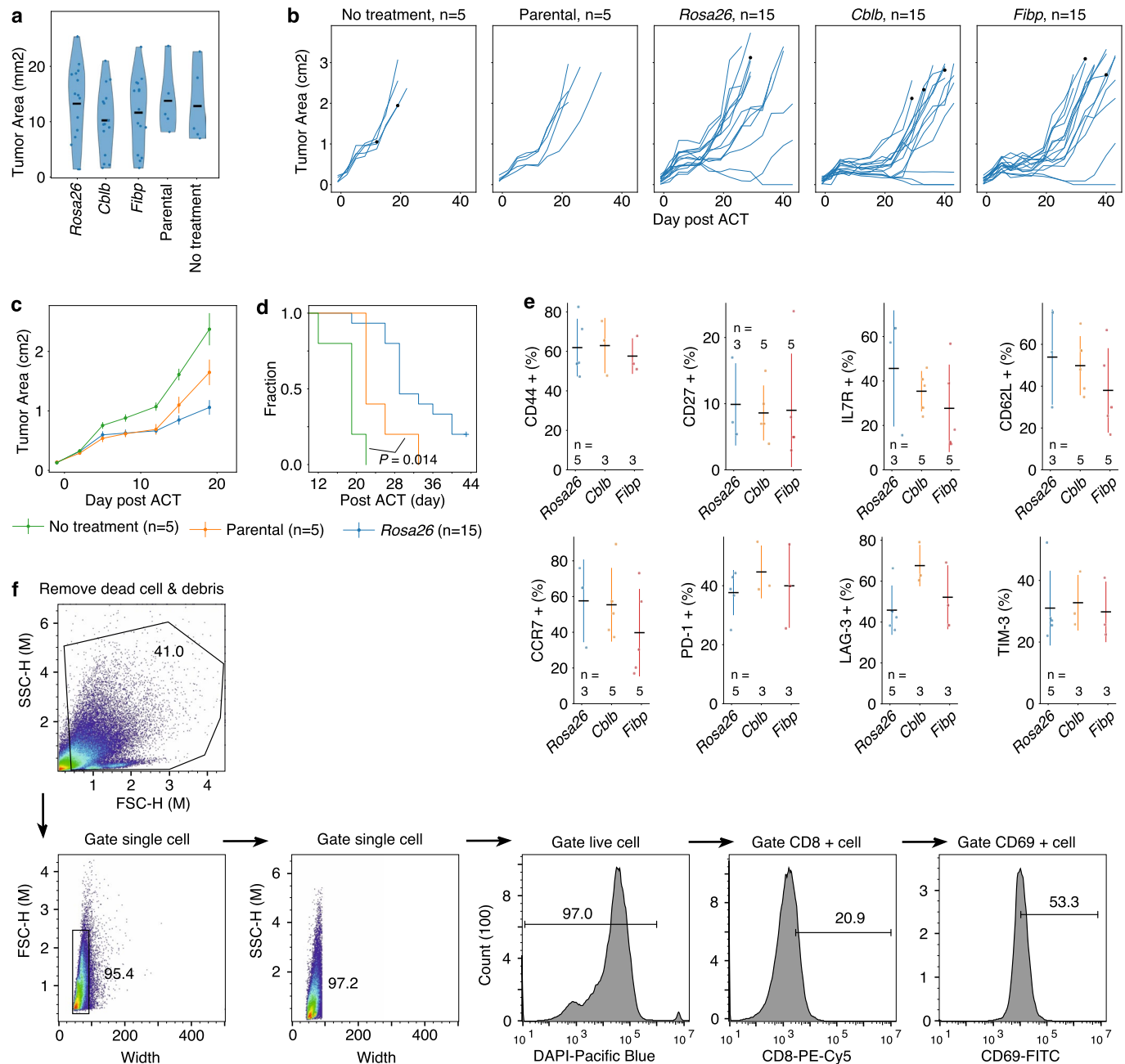
**Extended Data Fig. 4 | Control analyses of the median Tres signature in predicting immunotherapy responses.** **a**, Prediction through correlations between the median Tres signature and T-cell bulk transcriptomic profiles. **b**, Tres score correlations with profiles from post-treatment tumors. Each point represents an ICI-treated tumor. Y-axis presents the correlation between the Tres signature and T-cell expression profiles. P-values were from the two-sided Wilcoxon rank-sum test comparing group values. The thick line represents the median value. The bottom and top of the boxes are the 25th and 75th percentiles (interquartile range). Whiskers encompass 1.5 times the interquartile range. **c**, Tres scores indicate T-cell clinical efficacy. The ROC curve presents false-positive rates against true-positive rates of predicting whether T cells are from responders or non-responders. The performance of diverse signatures was compared. **d**, Comparison among T-cell signatures in predicting clinical response. The negative predictive value was shown for T-cell efficacy signatures in Supplementary Table 3. All box-plots have the same format as panel b ( $n = 6$  independent datasets per box). **e**, Lack of associations between Tres score correlations and adoptive cell therapy efficacy in tumors with T-cell infiltration lower than average. The survival of patients upon adoptive T cell transfer was shown for tumors with positive or negative Tres score correlations. P-values were from the two-sided Wald test using continuous values. **f**, The performance of Tres on predicting ICI outcomes using bulk data. Each dot represents a pretreatment tumor transcriptomics cohort listed in Supplementary Table 4. The first group presents the results using all samples. The other two groups present results using tumors with positive or negative CTL levels. The Y-axis presents Cox-PH risk z-scores as the association between overall survival and Tres signature correlations. Box plots have the same format as panel b. P-values were computed through the two-sided Wilcoxon signed-rank test. **g**, Tres prediction performance on different combinations of treatments and sample sites in a triple-negative breast cancer study<sup>40</sup>. The area under the ROC curve (AUC) and confidence intervals were shown with 0.5 as the random expectation. **h**, Tres prediction performance in tumors when immuno-suppressive signals are lower than average. The data and box-plots are shown as panel f.



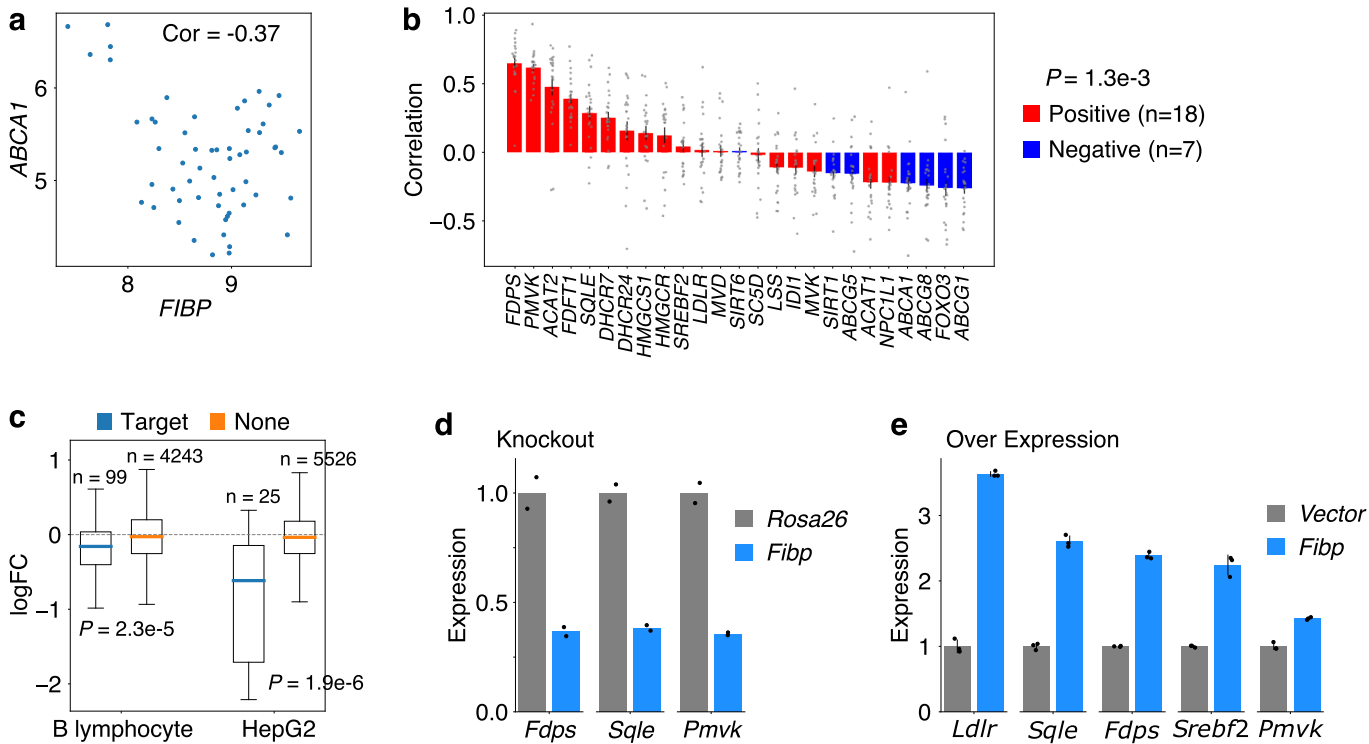
**Extended Data Fig. 5 | High *FIBP* levels in T cells are associated with inferior antitumor efficacy.** **a**, *FIBP* is the first among all genes based on the average rank across all signatures in Fig. 3a. **b**, High *FIBP* levels in bulk tumors indicate T-cell dysfunction, generated from the TIDE server<sup>68</sup>. For each neuroblastoma tumor<sup>78</sup>, the cytotoxic T-lymphocyte (CTL) infiltration level was estimated as the average expression level of CD8A, CD8B, GZMA, GZMB, and PRF1. Each Kaplan-Meier plot presents tumors in two groups: ‘CTL Top’ has above-median CTL values among all samples, while ‘CTL Bottom’ has values below the median. Samples were split according to the *FIBP* expression level through the best separation criterion maximizing the difference of associations between CTL and survival outcome between two groups.  $P$ -values are computed through the two-sided interaction t-test between CTL and *FIBP* using continuous values without any cutoffs. **c**, Only *Fibp* knockout (KO) promoted T-cell mediated cancer killing. Each gene was knocked out through a mixture of three independent gRNAs in Pmel-1 mouse T cells. The abundance of B16-mhgp100 co-cultured with gene KO T cells was measured as the intensity of tdTomato. The Y-axis presents the difference between each target gene KO and Rosa26 control KO. Each point presents the median and standard error of the mean as error bars ( $n=3$  cell-culture replicates). **d**, CRISPR screen phenotypes of *FIBP* compared to *CBLB*. Each dot represents a gRNA. The Y-axis shows the log<sub>2</sub> fold-change (logFC) of gRNA abundances between target and control conditions. Each condition presents mean and standard deviations as error bars across all independent gRNAs ( $n=4$  for the TCR stimulation screen<sup>12</sup>,  $n=6$  for the IL-2 production screen<sup>13</sup>).



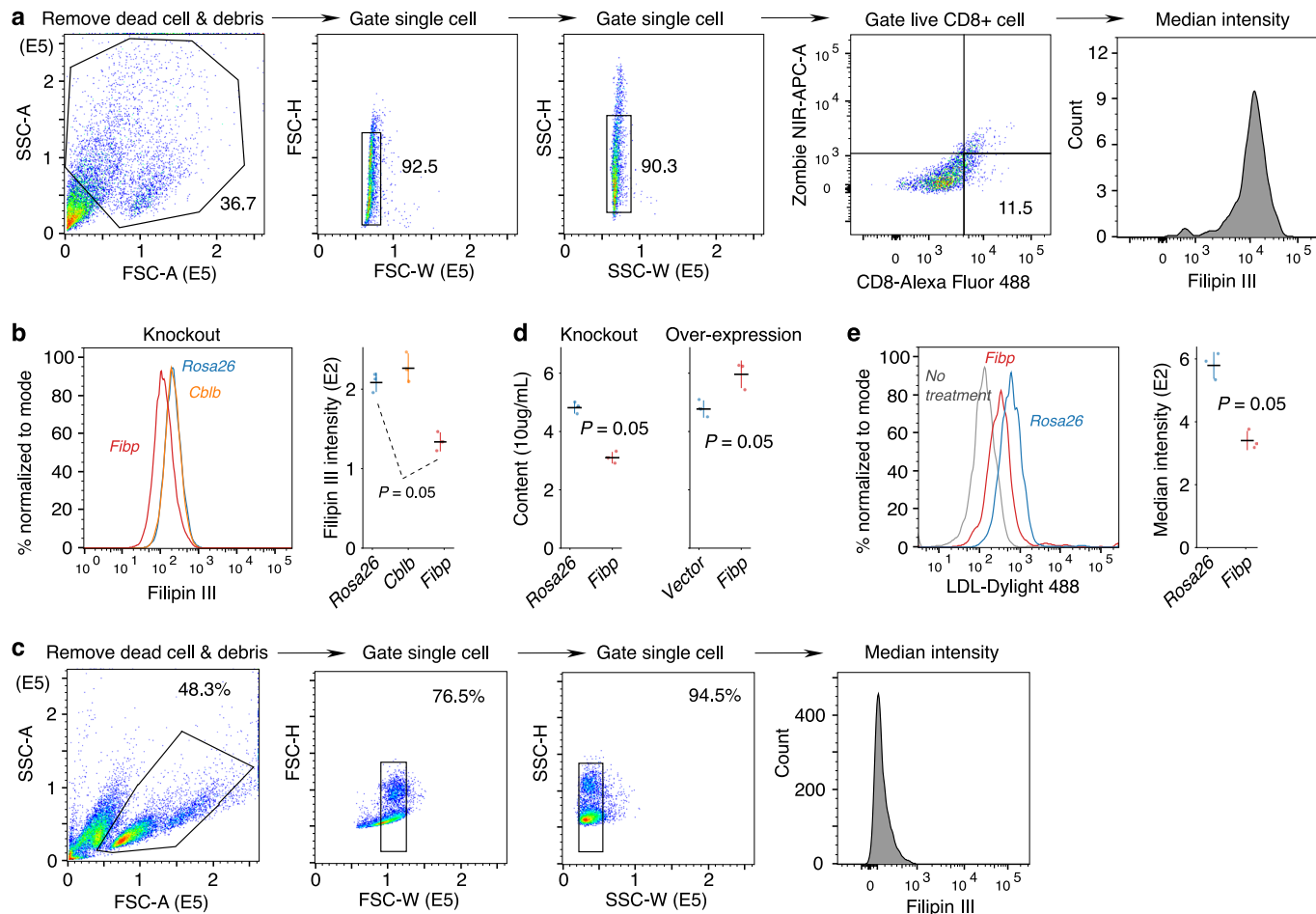
**Extended Data Fig. 6 | In vitro phenotypes of T cells after gene knockouts.** **a**, Efficacy of human donor T cells on killing A375 or Mel624 cells. The T-cell efficacy was measured as the relative red fluorescent protein (RFP) intensity (Y-axis) of cancer cells across time points (X-axis) as Fig. 4d. The culture conditions include three control gRNAs (AAVS1 for human and Rosa26 for mouse), parental T cells, and cancer cells cultured without T cells. For each condition, the mean and standard deviation (error bars) values were shown ( $n=3$  cell-culture replicates). **b**, Result from Pmel-1 TCR T cells on killing B16-mhgp100 cells, shown as panel a. **c**, Representative CFSE signals of T cell proliferation assay in Pmel-1 CD8+ T cells. The proliferative ability of Pmel-1 T cells were compared in Fibp knockout versus control cells (Rosa26 KO) after restimulation with anti-CD3/28 antibodies for 4 days. Representative CFSE signals from TCR stimulated and unstimulated T cells were shown. **d**, T cell proliferation assay in Pmel-1 CD8+ T cells. The mean and standard deviation values ( $n=3$  independent gRNAs) of the proliferation index for each gene were calculated using Flowjo software, with gating strategy in panel e. The comparison was through the two-sided Wilcoxon rank-sum test. **e**, Gating strategy for CFSE staining analysis. The forward-scatter area (FSC-A) and side-scatter area (SSC-A) are used for dead cell and debris removal. The forward-scatter height (FSC-H), width (FSC-W), side scatter height (SSC-H), width (SSC-W) are used to gate the single cells. We include the unstimulated T cells to define the background populations. Cells from all biological replicates in panel d are pooled together for demonstration. **f**, Early activation measured 12 h after TCR stimulation. CD69 level was determined by flow cytometry in FIBP and control KO cells in mouse and human. The left panel shows a representative histogram of signal intensity. The right panel shows the mean and standard deviations as error bars ( $n=3$  independent gRNAs per gene) for marker positive fractions. The comparisons between groups were through the two-sided Wilcoxon rank-sum test.



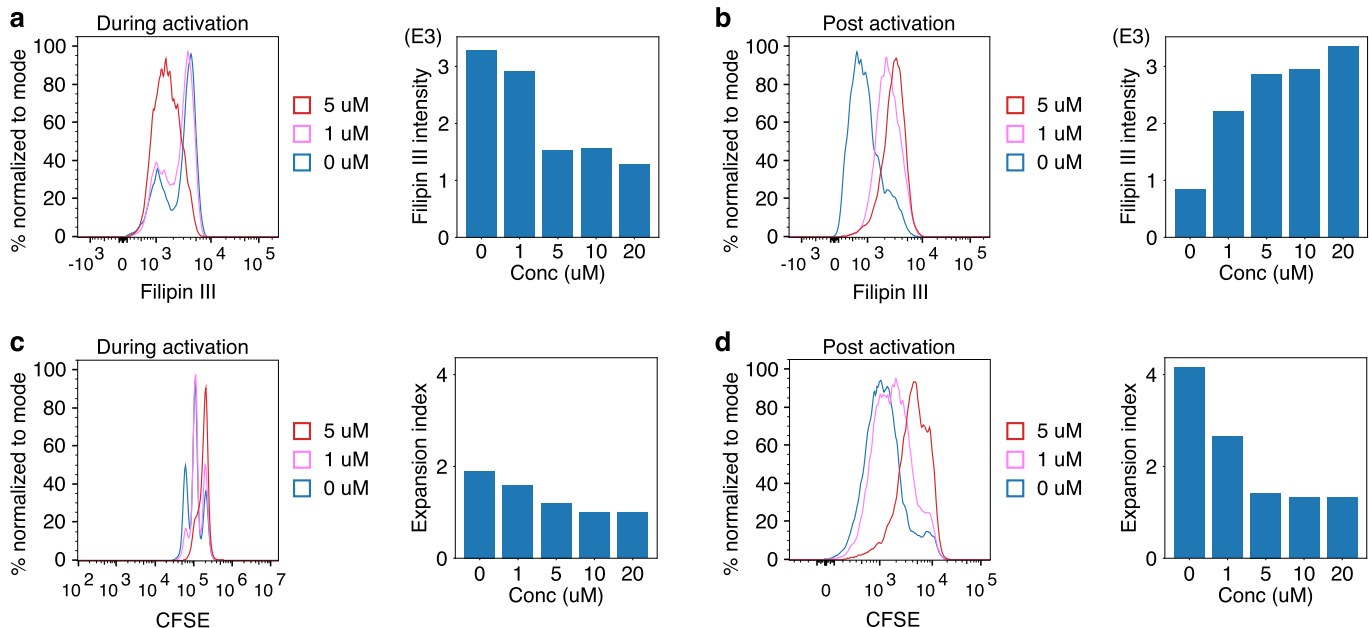
**Extended Data Fig. 7 | Analysis of T cells in adoptive cell transfer.** **a**, Tumor size in different groups randomized at day zero. All mice were randomized into different groups to achieve an even initial tumor size (n=15 for Rosa26, Cblb, and Fibp knockout (KO) groups, n=5 for parental and No treatment groups). The tumor area distribution was shown through violin plots smoothed with a kernel density estimator. **b**, Tumor size at different days post-adoptive cell transfer (ACT) for groups in panel a. **c**, Average tumor size in negative control groups. The tumor area mean was shown when no mice reached endpoints, with standard errors as error bars. **d**, Kaplan Meier curves of mice survival durations. The fraction of mice that did not reach the endpoint was shown on different days after ACT. The comparison of survival durations between no-treatment and parental groups was through the two-sided log-rank test. **e**, In-vivo flow analysis of T-cell phenotype markers. Marker positive fractions of T cells with gene KOs were shown with mean values and standard deviations as error bars (tumor counts labeled under each group, growth curves available in Supplementary Fig. 3). Different groups were compared through the one-sided Wilcoxon rank-sum test, and none of them achieved statistical significance. **f**, Gating strategy of in-vivo flow analysis. The forward scatter height (FSC-H) and side scatter height (SSC-H) are used for dead cell and debris removal. The forward scatter height (FSC-H), width (FSC-W), side scatter height (SSC-H), and width (SSC-W) are used to gate the single cells. DAPI was used to eliminate dead cells, and CD8+ cells were gated. Then marker positive cells (CD69 in this example) were gated on the basis of the non-staining control.



**Extended Data Fig. 8 | Differentially-expressed genes upon *FIBP* knockout are enriched for cholesterol metabolism functions.** **a**, Correlation between *FIBP* and *ABCA1* among acute lymphoblastic leukemia samples ( $n=58$ ) from the MILE project<sup>57</sup>. **b**, Mean and standard error (error bars) of correlations ( $n=22$  leukemia subtypes per bar) between *FIBP* and gene members in the cholesterol metabolism pathway. Gene members that positively or negatively regulate cholesterol metabolism were shown in red or blue colors, respectively. The comparison between the positive and negative groups is through the two-sided Wilcoxon rank-sum test. **c**, Differential expression values for SREBF2 ChIP-Seq targets and non-targets. The Cistrome database contains two public human ChIP-Seq profiles from B lymphocytes and HepG2 cells<sup>79</sup>. The regulatory score on each target gene is computed by the RABIT framework<sup>58</sup>. Target genes are those with regulatory scores larger than 0.5. None target genes are those with zero regulatory scores. The gene count in each group is labeled above each boxplot. The thick line represents the median value. The bottom and top of the boxes are the 25th and 75th percentiles (interquartile range). Whiskers encompass 1.5 times the interquartile range. The comparison between groups is through the two-sided Wilcoxon rank-sum test. **d**, RT-qPCR validation of essential enzymes in cholesterol synthesis in mouse T cells. Normalized expression levels were shown for *Rosa26* control and *Fibp* knockout conditions. The mean values were shown ( $n=2$  independent gRNAs). **e**, RT-qPCR levels of cholesterol metabolic regulators in mouse T cells with *Fibp* and vector control overexpression. The mean and standard deviation (error bars) were shown ( $n=3$  cell-culture replicates).



**Extended Data Fig. 9 | *Fibp* knockout reduces cholesterol levels in T cells.** **a**, Gating strategy of in-vivo Filipin III flow analysis. The forward scatter Area (FSC-A) and side scatter area (SSC-A) are used for dead cell and debris removal. The forward scatter height (FSC-H), width (FSC-W), side scatter height (SSC-H), and width (SSC-W) are used to gate the single cells. Live CD8+ T subset is gated on non-staining negative control and single staining positive control. The Filipin-III level was measured as the median fluorescence density. Cells from one example tumor are shown for demonstration. **b**, Cholesterol levels in *Fibp* versus *Rosa26* knockout (KO) T cells via Filipin III staining, with gating strategy in panel c. The left panel shows representative histograms of signal intensity. The right panel presents mean and standard deviation as error bars ( $n=3$  independent gRNAs). The  $p$ -value was from the two-sided Wilcoxon rank-sum test. **c**, Gating strategy of in vitro Filipin III analysis. The procedure is the same as panel a, except that the T-cell gating step is not involved as samples are in-vitro cultures of CD8+ T cells. **d**, Cholesterol levels via oxidation-based quantification. Each KO group has replicates from three independent gRNAs. Each overexpression group has replicates from three cell cultures. The data were presented and compared in the same way as panel b. **e**, LDL uptake after lipoprotein deprivation. CD8+ T cells with *Fibp* and *Rosa26* control KOs were treated with Dil-LDL after lipoprotein deprivation for 16 h. The LDL uptake was determined using flow cytometry. The left panel shows representative histograms. The right panel presents mean and standard deviation as error bars ( $n=3$  independent gRNAs).



**Extended Data Fig. 10 | Simvastatin does not inhibit cholesterol levels in activated T cells. (a, b)**, Cholesterol levels upon simvastatin treatments. T cells were treated with simvastatin concurrently with anti-CD3/28 activation (a, During) or 72 hours after anti-CD3/28 activation (b, Post). The median Filipin III intensity was measured with flow cytometry at different simvastatin concentrations, with a representative plot on the left and the median intensity on the right. The gating strategy follows the same scheme in Extended Data Fig. 9c. **(c, d)**, Simvastatin inhibits T-cell proliferation. For each condition, the T-cell expansion index was computed through CFSE staining and flow cytometry analysis. The data is shown in the same way as panels a, b.

Corresponding author(s): Peng Jiang

Last updated by author(s): Mar 22, 2022

## Reporting Summary

Nature Portfolio wishes to improve the reproducibility of the work that we publish. This form provides structure for consistency and transparency in reporting. For further information on Nature Portfolio policies, see our [Editorial Policies](#) and the [Editorial Policy Checklist](#).

### Statistics

For all statistical analyses, confirm that the following items are present in the figure legend, table legend, main text, or Methods section.

n/a Confirmed

- The exact sample size ( $n$ ) for each experimental group/condition, given as a discrete number and unit of measurement
- A statement on whether measurements were taken from distinct samples or whether the same sample was measured repeatedly
- The statistical test(s) used AND whether they are one- or two-sided  
*Only common tests should be described solely by name; describe more complex techniques in the Methods section.*
- A description of all covariates tested
- A description of any assumptions or corrections, such as tests of normality and adjustment for multiple comparisons
- A full description of the statistical parameters including central tendency (e.g. means) or other basic estimates (e.g. regression coefficient) AND variation (e.g. standard deviation) or associated estimates of uncertainty (e.g. confidence intervals)
- For null hypothesis testing, the test statistic (e.g.  $F$ ,  $t$ ,  $r$ ) with confidence intervals, effect sizes, degrees of freedom and  $P$  value noted  
*Give  $P$  values as exact values whenever suitable.*
- For Bayesian analysis, information on the choice of priors and Markov chain Monte Carlo settings
- For hierarchical and complex designs, identification of the appropriate level for tests and full reporting of outcomes
- Estimates of effect sizes (e.g. Cohen's  $d$ , Pearson's  $r$ ), indicating how they were calculated

*Our web collection on [statistics for biologists](#) contains articles on many of the points above.*

### Software and code

Policy information about [availability of computer code](#)

Data collection Python 3.8.8

Data analysis Python 3.8.8, Scipy 1.7.1, Django 4.0.1, MySQL 8.0.27, GCC 4.8.5, SDS 19.1, Flowjo 10.6.1, IPA v70750971, GSEA v4.2.3, CytoSig v0.1 (<https://github.com/data2intelligence/CytoSig>), The Tres model is available at <https://github.com/data2intelligence/Tres>. An interactive web server for Tres is available at <https://resilience.ccr.cancer.gov>. The programs for reproducing major results are available at [https://github.com/data2intelligence/Tres\\_main](https://github.com/data2intelligence/Tres_main).

For manuscripts utilizing custom algorithms or software that are central to the research but not yet described in published literature, software must be made available to editors and reviewers. We strongly encourage code deposition in a community repository (e.g. GitHub). See the Nature Portfolio [guidelines for submitting code & software](#) for further information.

### Data

Policy information about [availability of data](#)

All manuscripts must include a [data availability statement](#). This statement should provide the following information, where applicable:

- Accession codes, unique identifiers, or web links for publicly available datasets
- A description of any restrictions on data availability
- For clinical datasets or third party data, please ensure that the statement adheres to our [policy](#)

Data generated by this study: The RNA-Seq data was deposited to NCBI GEO with accession ID GSE186428. All flow analysis raw data are available in FCS format at the Flowrepository77 with accession IDs listed in Supplementary Table 10 and source data tables for each figure panel. All gene scores computed by the Tres model are available at <https://resilience.ccr.cancer.gov>.

**Public datasets:** Single-cell RNA-Seq data collected from public studies for training Tres signatures are listed in Supplementary Table 1. T-cell transcriptomic data for validating the Tres model is available for download as processed data at [https://github.com/data2intelligence/Tres\\_main](https://github.com/data2intelligence/Tres_main). Bulk-tumor transcriptomic datasets of ICI pretreatment tumors are listed in Supplementary Table 4. Public ChIP-Seq profiles of SREBF2 are originally available from GSE31477, and binding peak calls reprocessed by the Cistrome pipeline were available at <http://cistrome.org>. The CCLE cancer cell line expression profiles are available from <https://depmap.org>. Genome-wide CRISPR screen data on human donor T cells are downloaded from supplementary materials of the original studies (refs 12,13) and GSE174255. The MILE leukemia dataset is available from GSE13159.

**Public databases:** TIDE is available at <http://tide.dfci.harvard.edu>. Cistrome is available at <http://cistrome.org>. MSigDB, which provides KEGG gene sets (v7.4) of cell cycle and DNA replication, is available at <https://www.gsea-msigdb.org>.

Source data for all main and extended data figures are provided. Raw western blots are located in Supplementary Figure 1, Supplementary Figure 4, and Supplementary Figure 5. Raw IncuCyte images are located in Supplementary Figure 2.

## Field-specific reporting

Please select the one below that is the best fit for your research. If you are not sure, read the appropriate sections before making your selection.

Life sciences       Behavioural & social sciences       Ecological, evolutionary & environmental sciences

For a reference copy of the document with all sections, see [nature.com/documents/nr-reporting-summary-flat.pdf](https://nature.com/documents/nr-reporting-summary-flat.pdf)

## Life sciences study design

All studies must disclose on these points even when the disclosure is negative.

### Sample size

For our data integration work, no sample size calculation was performed because our data collection efforts are based on the available public data with predefined sample counts in each publication.

For the 1) in-vitro test of killing efficiency, cytokine secretion and proliferation assays of T cells after CRISPR editing (Fig. 4 and Extended Data Fig. 6), 2) the effect of cholesterol treatment (Fig. 6i), 3) In-vitro detection of CD69, Filipin III level, total cellular cholesterol contents and LDL uptake of T cells after CRISPR editing (Extended Data Fig. 6f, Extended Data Fig. 9b,d,e), no sample size calculation was performed. We chose a minimal sample size of 3, which is sufficient for the two-sided Wilcoxon rank-sum test to achieve a statistical significance of p-value 0.05 between groups with sufficient difference.

For adoptive T cell transfer therapy experiment (Fig. 5 and Extended Data Fig. 7a, b), no sample size calculation was performed. Instead, we selected the minimal mice sample size as 15. In fact, our recent study (Pubmed ID 29301958) demonstrated that 5-10 mice (smaller than our sample size 15) per group will be sufficient to compare treatment responses between conditions.

For the multidimensional flow analysis on CD8 TILs isolated from tumors (Fig. 5f, Fig. 6g, Extended Data Fig. 7e, Supplementary Figure 3), no sample size calculation was performed. For each markers panel, we include a minimal sample size of 3 in each treatment condition, which is sufficient for the two-sided Wilcoxon rank-sum test to achieve a statistical significance of p-value 0.05 between groups with sufficient difference.

All other analyses in this study are based on published datasets thus sample size selection is not relevant.

### Data exclusions

No data were excluded from our analyses.

### Replication

All experiments in this study are described in three parts below:

**In-vivo experiments:** For adoptive T cell transfer experiment (Fig. 5 and Extended Data Fig. 7a, b), we selected 15 replicates each gene knockout group. For the multidimensional flow analysis on CD8 TILs isolated from tumors (Fig. 5f, Fig. 6g, Extended Data Fig. 7e, Supplementary Figure 3), we include a minimal 3 replicates in each condition. The result is very close between replicates, which are all successful.

**In-vitro experiments:** We had three cell-culture replicates for the 1) in-vitro test of T cells killing efficiency after editing and effect of cholesterol to T cells function (Fig. 4, Fig. 6 and Extended Data Fig. 6), 2) Cholesterol metabolism study(qPCR, Filipin III detection, oxidation-based quantification of cholesterol levels) after Fibp knockout and over-expression (Fig. 6d, 6h, Extended Data Fig. 8d-e, Extended Data Fig. 9d). Cell-culture replicates are taken to monitor the performance of these experiments, so the replicate measurements are done at the same time. The result is quite consistent between replicates, which are all successful.

**Computational experiments:** Other experiments in this study are computational analyses using published datasets thus replication is not relevant because replication counts were already determined by each publication and cannot be changed by authors of this paper.

### Randomization

For adoptive T cell transfer therapy experiment, tumor-bearing mice were sub-lethally irradiated with the dose of 600 cGy, and then randomly distributed by shuffling their identities initially into different treatment groups (15 mice for each group, Fig 5 and Extended Data Fig 7a, b).

For the in-vitro experiment, randomization is not relevant because different editing and treatment conditions are applied on the same homogeneous pool of cells.

Other experiments in this study are computational analyses using published datasets thus randomization is not relevant because sample allocations are already determined by each publication and cannot be changed by authors of this paper.

## Blinding

For adoptive T cell transfer therapy experiment using C57BL/6 mouse, tumor size were measured in a double-blinded manner by the technician twice a week after T cell transfer and the tumor area was calculated as length\* width.

Blinding is not performed in other experiments because the robust phenotype of our result is based on strictly objective measurements by equipment instead of any human estimations.

## Reporting for specific materials, systems and methods

We require information from authors about some types of materials, experimental systems and methods used in many studies. Here, indicate whether each material, system or method listed is relevant to your study. If you are not sure if a list item applies to your research, read the appropriate section before selecting a response.

### Materials & experimental systems

n/a	<input type="checkbox"/> Involved in the study
<input type="checkbox"/>	<input checked="" type="checkbox"/> Antibodies
<input type="checkbox"/>	<input checked="" type="checkbox"/> Eukaryotic cell lines
<input checked="" type="checkbox"/>	<input type="checkbox"/> Palaeontology and archaeology
<input type="checkbox"/>	<input checked="" type="checkbox"/> Animals and other organisms
<input type="checkbox"/>	<input checked="" type="checkbox"/> Human research participants
<input checked="" type="checkbox"/>	<input type="checkbox"/> Clinical data
<input checked="" type="checkbox"/>	<input type="checkbox"/> Dual use research of concern

### Methods

n/a	<input type="checkbox"/> Involved in the study
<input checked="" type="checkbox"/>	<input type="checkbox"/> ChIP-seq
<input type="checkbox"/>	<input checked="" type="checkbox"/> Flow cytometry
<input checked="" type="checkbox"/>	<input type="checkbox"/> MRI-based neuroimaging

## Antibodies

### Antibodies used

Antibodies for Western blotting:  
 beta-Actin (Santa Cruz, sc-47778); Cbl-b antibody (G-1) (Santa Cruz, sc-8006)  
 Anti-FIBP antibody (Abcam, ab194793); SREBF2(1C6) antibody (Santa Cruz, sc-13552)  
 LDLR antibody (C7) (Santa Cruz, sc-18823)

Antibodies for flow cytometry:  
 PE anti-mouse CD3 (biolegend, 100205); FITC anti-mouse CD8 (biolegend, 100705);  
 PE anti-human CD3 (biolegend, 300307); FITC anti-human CD8 (biolegend, 344704);  
 PE anti-mouse CD197(CCR7) (BD Bioscience, 560682); PE-Cy7 anti-mouse CD62L (BD Bioscience, 560516);  
 APC anti-mouse CD27 (BD Bioscience, 560691); FITC anti-mouse CD69 (BD Bioscience, 561929);  
 PerCP-Cy5.5 anti-mouse CD44 (BD Bioscience, 560570); PE-Cy5 anti-mouse CD8a (BD Bioscience, 561094);  
 PE anti-mouse CD223(LAG-3) (biolegend, 125207); FITC anti-mouse CD279(PD-1) (biolegend, 135213);  
 APC anti-mouse CD366(Tim-3) (biolegend, 134007); PerCP-Cy5.5 anti-mouse IL7R (biolegend, 135021);

Antibodies for T cell activation:  
 anti-mouse CD3 (TONBO, 40-0032-U100, clone 17A2);  
 anti-mouse CD28 (TONBO, 40-0281-U100, clone 37.51);  
 anti-human CD3 (TONBO, 40-0038-U100, clone UCHT1);  
 anti-human CD28 (TONBO, 40-0289-U100, clone CD28.2);

### Validation

The antibodies for Western blotting, flow analysis and T-cell activation were all commercially available from Santa Cruz, BioLegend, Abvam, TONBO and BD Bioscience. Validation of antibodies has been performed by respective manufacturers, and validation notes are listed as follows:

#### Flow cytometry:

PE anti-mouse CD3, species reactivity:mouse. From manufacture's website: Each lot of this antibody is quality control tested by immunofluorescent staining with flow cytometric analysis.

FITC anti-mouse CD8, species reactivity:mouse. From manufacture's website: Each lot of this antibody is quality control tested by immunofluorescent staining with flow cytometric analysis.

PE anti-human CD3, species reactivity:human. From manufacture's website: Each lot of this antibody is quality control tested by immunofluorescent staining with flow cytometric analysis.

FITC anti-human CD8, species reactivity:human. From manufacture's website: Each lot of this antibody is quality control tested by immunofluorescent staining with flow cytometric analysis.

PE anti-mouse CD197, species reactivity:mouse. From manufacture's website: Flow cytometry (Routinely Tested)

PE-Cy7 anti-mouse CD62L, species reactivity:mouse. From manufacture's website: Flow cytometry (Routinely Tested)

APC anti-mouse CD27, species reactivity:mouse. From manufacture's website: Flow cytometry (Routinely Tested)

FITC anti-mouse CD69, species reactivity:mouse. From manufacture's website: Flow cytometry (Routinely Tested)

PerCP-Cy5.5 anti-mouse CD44, species reactivity:mouse. From manufacture's website: Flow cytometry (Routinely Tested)

PE-Cy5 anti-mouse CD8a, species reactivity:mouse. From manufacture's website: Flow cytometry (Routinely Tested)

PE anti-mouse CD223(LAG-3), species reactivity:mouse. From manufacture's website: Each lot of this antibody is quality control tested by immunofluorescent staining with flow cytometric analysis.

FITC anti-mouse CD279(PD-1), species reactivity:mouse. From manufacture's website: Each lot of this antibody is quality control tested by immunofluorescent staining with flow cytometric analysis.

APC anti-mouse CD366(Tim-3), species reactivity:mouse. From manufacture's website: Each lot of this antibody is quality control tested by immunofluorescent staining with flow cytometric analysis.

PerCP-Cy5.5 anti-mouse IL7R, species reactivity:mouse. From manufacture's website: Each lot of this antibody is quality control tested by immunofluorescent staining with flow cytometric analysis.

by immunofluorescent staining with flow cytometric analysis.

#### Western Blot:

beta-Actin, species reactivity:mouse/human, From manufacture's website: β-Actin (C4) antibody is tested by western blot analysis of β-Actin expression in HeLa, NIH/3T3 and KNRK whole cell lysates with the correct molecular weight of 43kDa.

Cbl-b antibody, species reactivity:mouse/human, From manufacture's website: Anti-Cbl-b Antibody (G-1) raised against amino acids 29-483 mapping at the N-terminus of Cbl-b of human and mouse origin, tested by western blot analysis of Cbl-b expression in BJAB, NAMALWA, Jurkat, CTLL-2 and TK-1 whole cell lysates with the correct molecular weight of 109kDa.

FIBP, species reactivity:mouse/human, From manufacture's website:anti-FIBP antibody is tested by western blot analysis of FIBP expression in SW620, MCF-7 and rat brain whole cell lysates with the correct molecular weight of 42kDa.

SREBF2(1C6) antibody,species reactivity:mouse/human, From manufacture's website: SREBF2(1C6) antibody raised against amino acids 833-1141 of SREBP-2 of human ,rat and mouse origin, tested by western blot analysis of SREBP-2 expression in HeLa, Caco-2 and AN3 CA whole cell lysates with the correct molecular weight of 125kDa.

LDLR antibody (C7), species reactivity:mouse/human, From manufacture's website: LDLR antibody (C7) is tested by western blot analysis of LDLR expression in Raji, NIH/3T3, c4, WEHI-231 and PC-12 whole cell lysates with the correct molecular weight of 160kDa.

## Eukaryotic cell lines

Policy information about [cell lines](#)

#### Cell line source(s)

A375 cells were purchased from American Type Culture Collection (ATCC, CRL-1619).

293FT cells were purchased from ThermoFisher (R70007).

Mel624 and B16-mhgp100 were kindly provided as a gift by Dr. Rigel J Kishton from the Surgery Branch at NCI, NIH. Mel624 cells were established in the Surgery Branch, NCI from resected tumors. B16 (H-2b), the original source of B16-mhgp100, is a gp100+ spontaneous murine melanoma obtained from the NCI tumor repository.

#### Authentication

We have confirmed with the commercial and collaborative sources from where the cells were obtained that cell lines were authentic and free of cross-contamination in 2019.

#### Mycoplasma contamination

All cell lines were tested negative for mycoplasma contamination.

#### Commonly misidentified lines (See [ICLAC](#) register)

No commonly misidentified cell lines were used.

## Animals and other organisms

Policy information about [studies involving animals; ARRIVE guidelines](#) recommended for reporting animal research

#### Laboratory animals

C57BL/6 mice were purchased from the Charles River Laboratories (NCI strains). Female mice at 6-8 weeks of age were used for tumor incubation and T cell transfer experiments.

Pmel-1 T cell receptor (TCR) transgenic mice (Female, 8 weeks) were provided as a gift by Dr. Chi-Ping Dai from Merlino Lab at NCI, NIH. Mice were housed on 12 h light:dark cycles with the ambient temperature at 20–25 °C and 40-60% humidity.

#### Wild animals

This study did not involve wild animals.

#### Field-collected samples

This study did not involve samples collected from the field.

#### Ethics oversight

All animal experiments were approved by the NCI Animal Ethics Committee of NIH and performed strictly according to the animal protocol CDSL-001, or conducted under protocol 4924-19, approved by the Committee of the Use of Live Animals in Teaching and Research at the University of Hong Kong.

Note that full information on the approval of the study protocol must also be provided in the manuscript.

## Human research participants

Policy information about [studies involving human research participants](#)

#### Population characteristics

Healthy donors above eighteen years old without any immune system disorders are included in this study.

#### Recruitment

Health donors who are giving a volunteered blood donation were recruited in this study.

#### Ethics oversight

All PBMCs used for transduction were obtained from healthy donors on NCI IRB-approved protocols.

Note that full information on the approval of the study protocol must also be provided in the manuscript.

# Flow Cytometry

## Plots

Confirm that:

- The axis labels state the marker and fluorochrome used (e.g. CD4-FITC).
- The axis scales are clearly visible. Include numbers along axes only for bottom left plot of group (a 'group' is an analysis of identical markers).
- All plots are contour plots with outliers or pseudocolor plots.
- A numerical value for number of cells or percentage (with statistics) is provided.

## Methodology

### Sample preparation

#### 1, Preparation of human and mouse donor T cells:

Human NY-ESO-1 CD8+ T cells were stimulated with plate-bound anti-human CD3 (TONBO, 40-0038-U100, clone UCHT1) at 10 ug/mL and anti-human CD28 (TONBO, 40-0289-U100, clone CD28.2) at 2 ug/mL for 48 hours before expanded with recombinant human IL-2 (Biologend, 589106) at 100 IU/mL. Cells were cultured in completed X-Vivo medium, which is X-Vivo 15 Serum-free Hematopoietic Cell Medium (Lonza, BE02-060Q) supplemented with 5% inactivated fetal bovine serum (Gibco, 10082147), 50uM 2-mercaptoethanol (Gibco, 21985023), and 10mM N-Acetyl L-cysteine (Sigma, A7250-5G) at 1E6 cells/mL.

CD8+ T cells were isolated from the single-cell suspension of splenocytes of Pmel-1 TCR transgenic or regular mice using the EasySep mouse CD8+ T cell isolation kit (STEMCELL, Cat# 19853) by magnetic negative selection. If cells were not used directly, the freshly isolated splenocytes would be frozen in cryopreservation medium (Gibco, Cat# 2176664). CD8+ T cells isolated from newly-thawed splenocytes using the same method were rested in the medium overnight before stimulation. Isolated CD8+ T cells were stimulated with plate-bound anti-mouse CD3 (TONBO, 40-0032-U100, clone 17A2) at 10 ug/mL and anti-mouse CD28 (TONBO, 40-0281-U100, clone 37.51) at 5 ug/mL for 48 hours before expanded with recombinant mouse IL-2 (Biologend, 575406) at 100 IU/mL.

Pre-activated mice or human CD8+ T cells were spun down and resuspended in the Lonza P3 buffer at 1E6 cells/ 20 uL and added 60 uL cell resuspension to the PCR tube. The cells/ Cas9-RNP mixture were transferred to the 100 uL nucleofection cuvette (Lonza, V4XP-3024) and electroporated using the pulse program CM137 for mice activated T cells and EH100 for human activated T cells. After nucleofection, immediately added 100 uL pre-warmed culture medium to the cuvettes and transferred the cells to a 6-well plate at the density of 1E6 cells/mL. Evaluation studies of surface and intracellular markers on CD8+ T cells after crispr editing were performed at indicated timepoints.

#### 2, In vivo multi-panel flow analysis of tumor-infiltrating CD8+ T cells:

Tumors were collected on day 9-12 after CD8 T cell transfer, manually minced and incubated in RPMI 1640 medium containing DNase I (200 ug/mL, Sigma, DN-25) and Liberase™ (100 ug/mL, Sigma, 5401020001) for 30 mins at 37 °C. The dissociated cells were then passed through the 70 uM cell strainer (BD Falcon, 352350). CD8+ T cells were then enriched from the filtered cells using the CD8 TIL microbeads (Miltenyi, 130-116-478) according to the manufacturer's instructions. Cells were then stained with the indicated cell surface antibodies, DAPI was used to identify dead cells. For Filipin III staining, dead cells were marked using Zombie NIR fixable viability kit (Biologend, 423105) before fixation and staining.

Tumors with sizes of less than 10 mm<sup>2</sup> were excluded from analysis because the amount of tumor-infiltrating T cells was not sufficient for flow cytometry. The maximum tumor diameter permitted by animal committees is 2 cm, and this maximum tumor size was not exceeded.

#### 3, In vitro analysis of mouse T cells upon Statin treatment:

Simvastatin (sigma, PHR1438) was provided as solid powder and dissolved in DMSO at the stock concentration of 20 mM at -80°C. CD8 T cells isolated from C57BL/6 mice splenocytes were stained with CFSE dye as described above, then stimulated with anti-mouse CD3/28, and treated with simvastatin at indicated concentrations simultaneously. Same CFSE staining and treatment of simvastatin was applied to CD8 T cells after stimulation and during expansion with IL2 for 3 days. At the end of treatment, cells were collected and washed before Filipin III and CFSE detection by flow cytometry.

### Instrument

ACEA Novocyte Quanteon; BD LSR Fortessa SORP I;FACS Cantoll analyzer;BD FACSsymphony

### Software

FlowJo 10.6.1

### Cell population abundance

The median intensities among cell populations, or positive fractions were shown and compared within each figure (Fig 5f, 6g-h, Extended Data Fig 6c-d, 6f, Extended Data Fig 7e, Extended Data Fig 9b, 9e, Extended Data Fig 10).

### Gating strategy

We used the forward scatter area or height (FSC-A or FSC-H), and side scatter area or height (SSC-A or SSC-H) for dead cell and debris removal. The forward scatter height (FSC-H), width (FSC-W), side scatter height (SSC-H), width (SSC-W) are used to gate the single cells. For the analysis on CD8 TILs, we further include DAPI/ Zombie NIR and CD8 to identify live CD8 T cells. We include unstained cells to define the threshold that separates positive populations from negative control cells. Gating strategies were demonstrated in Extended Data Fig 6e, 7f and Extended Data Fig 9a and 9c.

- Tick this box to confirm that a figure exemplifying the gating strategy is provided in the Supplementary Information.